Summer 2014

Microwave assisted reconstruction of optical interferograms for distributed fiber optics sensing & characterization of PCB dielectric properties using two striplines on the same board

Lei Hua

Recommended Citation

Hua, Lei, "Microwave assisted reconstruction of optical interferograms for distributed fiber optics sensing & characterization of PCB dielectric properties using two striplines on the same board" (2014). *Masters Theses*. 7312.
https://scholarsmine.mst.edu/masters_theses/7312

MICROWAVE ASSISTED RECONSTRUCTION OF OPTICAL INTERFEROGRAMS FOR DISTRIBUTED FIBER OPTICS SENSING & CHARACTERIZATION OF PCB DIELECTRIC PROPERTIES USING TWO STRIPLINES ON THE SAME BOARD

By

LEI HUA

A THESIS

Presented to the Faculty of the Graduate School of the

MISSOURI UNIVERSITY OF SCIENCE AND TECHNOLOGY

In Partial Fulfillment of the Requirements for the Degree

MASTER OF SCIENCE IN ELECTRICAL ENGINEERING

2014

Approved by

Dr. Hai Xiao, Advisor
Dr. Jun Fan, Co-advisor
Dr. Hai-Lung Tsai

PUBLICATION THESIS OPTION

This thesis consists of one article that has been formatted according to the university's spec of thesis. Pages 48-69 have been accepted to be published in 2014 on IEEE International Symposium on Electromagnetic Compatibility, Raleigh, NC.

ABSTRACT

A new concept, the microwave-assisted reconstruction of an optical interferogram for distributed sensing, was developed to resolve both the position and reflectivity of each sensor along an optical fiber. This approach involves sending a microwave-modulated optical signal through cascaded fiber optic interferometers. The optical spectrum of each sensor can be reconstructed by sweeping the optical wavelength and detecting the modulation signal. A series of cascaded fiber optic extrinsic Fabry-Perot interferometric sensors was used to prove the concept. The microwave-reconstructed interferogram matched well with those recorded individually from a traditional optical spectrometer. The application of distributed strain measurement was also investigated. The wavelength shift of the interferogram increases linearly as a function of the applied strain, and the increasing strain did not incur noticeable loss in the reflection spectra.

ACKNOWLEDGEMENT

I would like to take this opportunity to thank all those people who helped me with the successful completion of my research. First, I would like to express my gratitude to my advisor Dr. Hai Xiao and my co-advisor Dr. Jun Fan. I thank them for giving me a chance to work with the group and for providing me financial support. Without their continued support with valuable advice and encouragement, this research could be considered incomplete. Their hard-work and patience have made a great impact on this research and me.

I am grateful to Dr. Hai-Lung Tsai, Department of Mechanical and Aerospace Engineering for being my committee member.

I also would like to take this opportunity to thank the colleagues in my group for being supportive all the time.

I thank my parents and my friends, for everything they have done for me. They have impacted and encouraged me to be the best person I can be.

TABLE OF CONTENTS

Page

PUBLICATION THESIS OPTION iii

ABSTRACT iv

ACKNOWLEDGEMENT v

LIST OF ILLUSTRATIONS ix

LIST OF TABLES xi

SECTION

1. INTRODUCTION 1

  1.1. BACKGROUND 1

  1.2. A NOVEL CONCEPT: A DISTRIBUTED SENSING NETWORK 2

    1.2.1. Review of the Relevant Technologies 2

      1.2.1.1 A networked sensor 2

      1.2.1.2 Multipled sensors. 3

      1.2.1.3 Time and frequency domain reflectometry 5

    1.2.2. The Microwave-assisted Reconstruction of an Optical Interferogram for Distributed Sensing 6

  1.3. RESEARCH OBJECTIVE 8

  1.4. THESIS OVERVIEW 8

2. FUNDAMENTAL PHYSICS 9

  2.1. FUNDAMENTAL PHYSICS OF FABRY-PEROT INTERFEROMETER (FPI) 9

  2.2. OPTICAL FIBER-BASED LOW FINESSE EXTRINSIC FABRY-PEROT INTERFEROMETER (EFPI) 14

  2.3. SENSING MECHANISM OF OPTICAL FIBER-BASED EFPI 17

        2.3.1. Strain Sensing Mechanism of EFPI 17

        2.3.2. EFPI’s Temperature Sensing Mechanism 18

    2.4. CONCEPT OF MICROWAVE-ASSISTED RECONSTRUCTION OF OPTICAL INTERFEROGRAMS 18

3. SYSTEM IMPLEMENTATION AND OPTIMIZATION 21

    3.1. OPTIMIZE THE INTERROGATION SYSTEM 21

        3.1.1. EOM-based Amplitude Modulation. 21

        3.1.2. Adjust the Input Polarization State to Optimize the Modulation Depth 23

    3.2. CONTROL OF THE COHERENT LENGTH IN BOTH AN OPTICAL AND A MICROWAVE DOMAIN USED TO REALIZE LIGHT SIGNAL’S DISTRIBUTED CAPABILITY 27

        3.2.1. Introduction of Coherence Length 27

        3.2.2. Maximize the Microwave Coherence Length and Minimize the Optical Coherence Length 28

    3.3. VALIDATE THE INTERROGATION SYSTEM 28

        3.3.1. System Realization 28

        3.3.2. Design and Fabrication of Optical Fiber Based EFPI 31

        3.3.3. Reconstruction of Optical Interferograms Using Cascaded EFPIs 33

4. EXPERIMENTAL RESULTS 38

5. CONCLUSIONS AND FUTURE WORK 42

    5.1. CONCLUSIONS 42

    5.2. FUTURE WORK 43

BIBLIOGRAPHY 44

PAPER

CHARACTERIZATION OF PCB DIELECTRIC PROPERTIES USING TWO STRIPLINES ON THE SAME BOARD……………………………………………48

ABSTRACT 48

1. INTRODUCTION 49

2. METHODOLOGY 51

    2.1. TRL CALIBRATION AND MEASUREMENT RESULT 52

    2.2. METHODOLOGY FOR MATERIAL PROPERTY EXTRACTION FROM MEASUREMENT S-PARAMETER 55

        2.2.1. “Root-omega” Method 58

        2.2.2. Assume the Conductors are Rough 59

3. RESULTS AND DISCUSSION 63

4. CONCLUSION 68

BIBLIOGRAPHY 69

VITA 70

LIST OF ILLUSTRATIONS

SECTION Page

Figure 1.1 Schematic diagram of spatial multiplexing 3

Figure 1.2 Schematic diagram of the series multiplexing.. 4

Figure 1.3 Schematic of the distributed fiber optical sensing concept through a microwave reconstructed optical spectra. 7

Figure 2.1 Fabry-Perot interferometer 9

Figure 2.2 Reflectance $\boldsymbol{R}$ of FPI as a function of the round-trip phase difference $\boldsymbol{\delta}$ for the increasing reflection coefficient $\boldsymbol{r}$.. 14

Figure 2.3 Schematic of the EFPI 15

Figure 3.1 EOM schematic 22

Figure 3.2 Optical power out (dB) versus modulator DC bias voltage (V) 22

Figure 3.3 Schematic of a fiber in-line polarizer 24

Figure 3.4 Schematic of a three waveplates polarization controller 24

Figure 3.5 Schematic of the modulation depth arrangement 25

Figure 3.6 A modulation depth waveform as detected by an oscilloscope.. 26

Figure 3.7 Schematic of an interrogation system for distributed fiber optic sensing. 28

Figure 3.8 Two points of view of the experiment arrangement.. 30

Figure 3.9 In-line EFPI Sensor as seen through the microscope 33

Figure 3.10 Time domain signal after applying a complex inverse Fourier transform to the microwave spectrum at 1553 nm and microwave reconstructed optical interferogram of the three EFPIs versus their spectra taken individually from the OSA, respectively.. 34

Figure 4.1 Strain distribution of an optical fiber with three multiplexed EFPI sensors ... 39

Figure 4.2 Resonant wavelength shift of the second EFPI sensor as a function of applied strain. 39

Figure 4.3 Shift in spectra of the second EFPI as strain increased 40

PAPER

Figure 1 Top view of the traces with different widths, with the broad trace also having shielding vias; Cross-sectional view of the two traces with different widths 52

Figure 2 TRL calibration standard details. 54

Figure 3 TDR measurement of all TRL standards and the DUT showing two big bumps representing the inductive via. 54

Figure 4 S-parameters of two traces over several repetitions of measurements........... 55

Figure 5 Methodology of material property extraction with the thread on the left assumes the conductor is smooth (root omega method) and the thread on the right accounts for roughness and separates it from the dielectric parameters. 57

Figure 6 Rough conductor cross-section showing the different dimensions and roughness parameters. 61

Figure 7 Narrow trace cross-section observed under a metallographic microscope shows the trace and reference planes with the relevant dimensions marked on the image. 63

Figure 8 Dk found using root omega method and proposed new method with a difference of about 16% between the two methods at 10 GHz....................... 64

Figure 9 Dk found using root omega method and proposed new method with a difference of about 18% in root omega method results from different traces and 30% between the two methods at 10 GHz.................................... 65

LIST OF TABLES

PAPER Page

Table 1 Values of the Trace Cross-Sectional Analysis Parameters Averaged Over the Measurements from Three Samples.. 63

1. INTRODUCTION

1.1. BACKGROUND

Fiber optic sensor technology is a novel sensing technology which is developed with the optical fiber communication. Fiber optic sensors have several key advantages over conventional sensing approaches. They are smaller, lighter, and immune to electromagnetic interference. They have harsh environment capabilities, are highly sensitive, possess good chemical stability, are geometrically adaptable, and have a distributed sensing capability. These properties allow both the detection and control of either long distance or multi-path to be implemented with an optical fiber sensor. In recent years, optical fiber sensing technology has experienced rapid development with numerous applications in the aerospace industry, biochemical industry, military equipment, and transportation.

Distributed fiber optic sensors are becoming the most popular technology due to both their detection capabilities on the uninterrupted spatial and real-time measurement of the structure’s health.

The potential incidents of large size civil structures i.e., buildings, bridges, dams, tunnels, pipelines and offshore platforms would bring overwhelming impacts on not only the economy but also human lives. Every year the government spends billions of dollars to maintain the aging structures. Factors that may cause collapse must be accurately predicted to reduce the economic impact. Using sensors in Structure Health Monitoring (SHM) [1-4] is considered one of the most reliable, efficient prediction methods currently available. SHM is the process of implementing a damage detection and characterization strategy for engineering structures.

Most civil infrastructures today include a complex geometry with large dimensions. Thus, the structure health evaluation is requested to be an in-one-piece distributed sensing to provide spatially-continuous information all along the whole structure. In contrast, damage detection requires distributed sensing techniques with a high measurement resolution, a large dynamic range, and a robust system. In general, spatially distributed information can be acquired by either grouping/multiplexing a large number of discrete sensors or by sending a pulsed signal to probe the spatially resolved information as a function of time-of-arrival.

1.2. A NOVEL CONCEPT: A DISTRIBUTED SENSING NETWORK

1.2.1. Review of the Relevant Technologies. The optical signal's amplitude, phase, polarization, and spectral information of the optical signal in a point sensor element can typically be measured. Spatially distributed information can be obtained from these measurements, and it can also be obtained through either the frequency or time domain light modulation. The following section summarizes a number of existing techniques, their latest advancements, and their limitations for distributed sensing.

1.2.1.1 A networked sensor. A large number of point sensors can be grouped together to form a monitoring network.

Within this network, the sensors are deployed at different locations, uniquely indexed, and connected/ interrogated through either a wireless or a wired link [10-13]. For example, the dynamic behavior of large-scale civil infrastructures was monitored under both normal and post-disaster conditions using the dense deployment of wireless smart sensors. The unique advantages of networked sensors include flexibility in sensor deployment, heterogeneity in sensor functions (i.e., inclusion of different types of sensors), and a hierarchy in group formation. In contrast, networked sensors provide only discrete sampling of the space, leaving dark zones in SHM. Additionally, such a monitoring network is complex, data massive, and difficult to manage.

1.2.1.2 Multipled sensors. Multiplexing involves four primary functions: powering, detecting, identifying, and evaluating. The basic multiplexing topology chosen is dependent on the sensing technology used [14, 15]. Multiplexed topologies include two main categories: spatial multiplexing and serial multiplexing. Spatial multiplexing (see Fig.1.1) consists of one optical fiber strand per optical fiber sensor, one source and one detector. Typical spatial multiplexing topologies include a reflective star and a reflective tree.

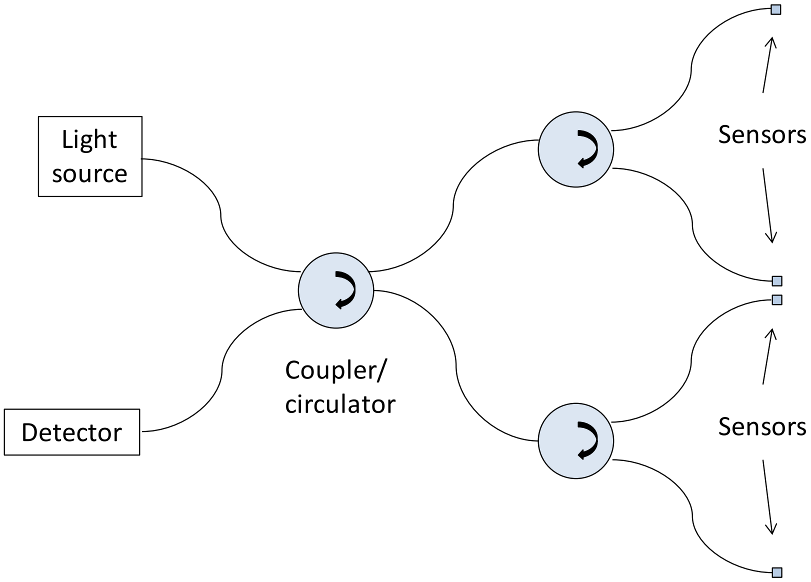

Figure 1.1 Schematic diagram of spatial multiplexing

Serial multiplexing consists of a number of optical fiber sensors connected end-to-end along a continuous fiber (see Fig.1.2). It is useful for measuring not only the magnitude but also its variation along the length of the fiber.

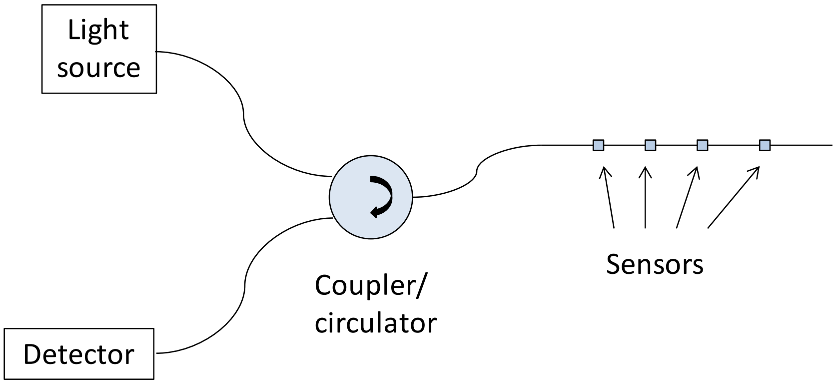

Figure 1.2 Schematic diagram of the series multiplexing

A single optical fiber may contain many sensors in a series to monitor the desired parameter’s distribution along the entire fiber. This process is known as quasi-distributed sensing. These sensors have unique signatures (e.g., different wavelength) that can be unambiguously identified with a single interrogation unit [16, 17]. This method is commonly referred to as multiplexed sensing. Multiplexed Fiber Bragg Gratings (FBGs) have been widely used in SHM to acquire spatially sampled information with high measurement resolutions [18, 19]. Unfortunately, the maximum number of FBG sensors along an optical fiber is limited by both the bandwidth of the light source and the required frequency interval per sensor to prevent overlapped signals and crosstalk. Recently, a wavelength scanning time division multiplexing interrogated 1000 ultra-weak FBGs for distributed temperature sensing [20, 21]. The time domain measurement, however, produced a great deal of system noise. Additionally, the signal needed to be accumulated multiple times to achieve a better signal-to-noise ratio (SNR).

1.2.1.3 Time and frequency domain reflectometry. Another technique, known as Time Domain Reflectometry (TDR), has also explored the spatially continuous sensing of various parameters in SHM [22-25]. In TDR, a pulsed signal is sent along a cable, and the time/space resolved reflections are collected and analyzed. These reflections can be from Rayleigh, Brillouin, and Raman scatterings. For example, a long-range spatially continuous Brillouin Optical Time-Domain Analysis (BOTDA) measurement system was demonstrated with a spatial resolution of 2m over a sensing length of 100km. The unique advantages of TDR-based distributed sensing include both a long coverage span and spatial continuity. The measurement resolution of TDR, however, is generally low as a result of inherently weak scatterings. Additionally, the spatial resolution of TDR is approximately 0.5m. It is limited by the pulse width of the interrogation signal.

Optical Frequency Domain Reflectometry (OFDR) was proposed to improve not only SNR but also the spatial resolution of TDR [26, 27]. In OFDR, both a frequency-scanning, highly coherent source and a Michelson interferometer are used to encode the time-of-arrival information into frequency domain signals. These signals can then be Fourier-transformed back to a time/space domain. Both the SNR and the spatial resolution of OFDR method are noticeably higher than the traditional TDR method. OFDR is also the possibility of narrow-bandwidth operation. OFDR broadband detectors are required to resolve the pulse lengths of a few tens of nanoseconds. The transfer function, however, is determined point wise for each modulation frequency. Thus, only one frequency component can be measured at each time. The use of narrow-bandwidth detectors improves the signal-to-noise-ratio. Measurement accuracy, however, is limited by the power fluctuations and/or random changes in polarization. Additionally, the measurement distance of OFDR is approximately several hundred meters due to the availability of high-quality light sources with both long coherence length and fine frequency scanning intervals [28].

1.2.2. The Microwave-assisted Reconstruction of an Optical Interferogram for Distributed Sensing. The light from a low coherence light source (broadband source) is launched into a tunable filter and then amplitude-modulated by a microwave signal. This signal’s modulation frequency can be scanned via computer control. The microwave-modulated light where the optical is the carrier and the microwave is the envelope is then sent into an optical fiber, with cascaded, reflective sensors, through a fiber-optic circulator (see Fig.1.3). The reflection of each sensor can be designed to be weak enough that the light is transmitted over many sensors but the multiple reflections within each sensor can be negligible. The coherence length of the light, which is determined by the bandwidth of the tunable filter, is much larger than the optical path differences (OPD) of the EFPI sensors but much smaller than the distance between two adjacent sensors. As a result, optical interference occurs within one sensor while the optical interference between sensors is avoided. These reflections travel backwards, pass the fiber circulator, and are detected by a high-speed photodetector (PD). Optical detection is synchronized with the microwave frequency by a Phase Lock Loop (PLL) so that the amplitude and phase of each reflected signal can be uniquely resolved. The reflection spectrum (with both amplitude and phase) can be obtained after the microwave frequency is scanned throughout the entire available range. The reflection spectrum (with both amplitude and phase) is obtained. The inverse complex Fourier transform of reflection spectrum provides the time-resolved discrete reflections along the fiber. After that, by sweeping the optical carrier wavelength using the tunable filter and recording every time-resolved discrete reflection signal in different optical wavelength, the optical spectrum for each sensor can be reconstructed simultaneously.

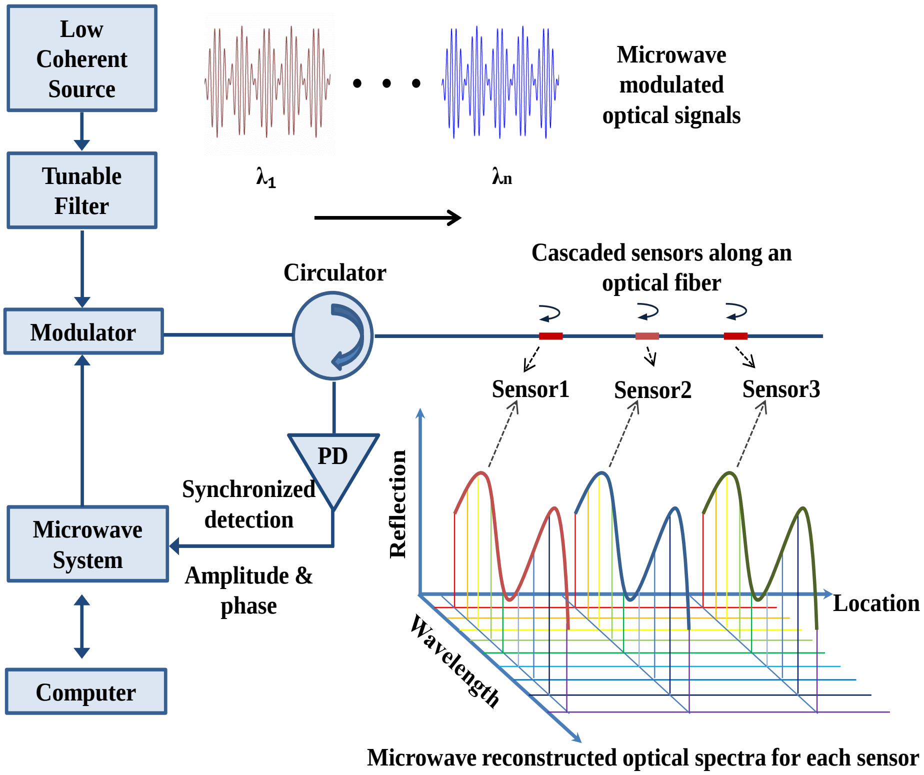

Figure 1.3 Schematic of the distributed fiber optical sensing concept through a microwave reconstructed optical spectra (PD: photo-detector)

1.3. RESEARCH OBJECTIVE

This research was conducted to investigate the microwave-assisted reconstruction of optical interferograms for distributed fiber optic sensing. The objectives of this study included the following:

- Understand both the physical insights and the sensing mechanism of EFPI
- Implement, validate, and optimize the interrogation system to achieve maximum distributed sensing capabilities with high measurement resolutions
- Measure distributed strain response based on cascaded EFPIs

1.4. THESIS OVERVIEW

This thesis focuses on the study of distributed fiber optic sensing techniques through microwave reconstructed optical spectra. The contents of this discussion are arranged into four sections:

Section 2 focuses on the fundamental physics of the FPI, the EFPI, and the distributed sensor.

Section 3 discusses the development of the microwave-assisted reconstruction of optical interferograms for distributed fiber optics sensing. The discussion includes the optimization the modulation depth of the EOM, the selection of the light source.

Section 4 analyzes the experimental results taken from the EFPIs, including the spectra’s reconstruction and the strain test.

Section 5 includes both a summary of this work as well as suggestion for future studies.

2. FUNDAMENTAL PHYSICS

2.1. FUNDAMENTAL PHYSICS OF FABRY-PEROT INTERFEROMETER (FPI)

A Fabry–Perot interferometer’s (FPI) foundation is a pair of partially reflective glass optical flats spaced either millimeters or centimeters apart with the reflective surfaces facing away from each other. A pair of either thick glass or quartz plates is used to include air between the flats (see Fig. 2.1). Beams of light are then reflected several times within the formed air. The entire structure is often known as a cavity. The thickness (*d*) of the air cavity is an important parameter of the interferometer[29-31].

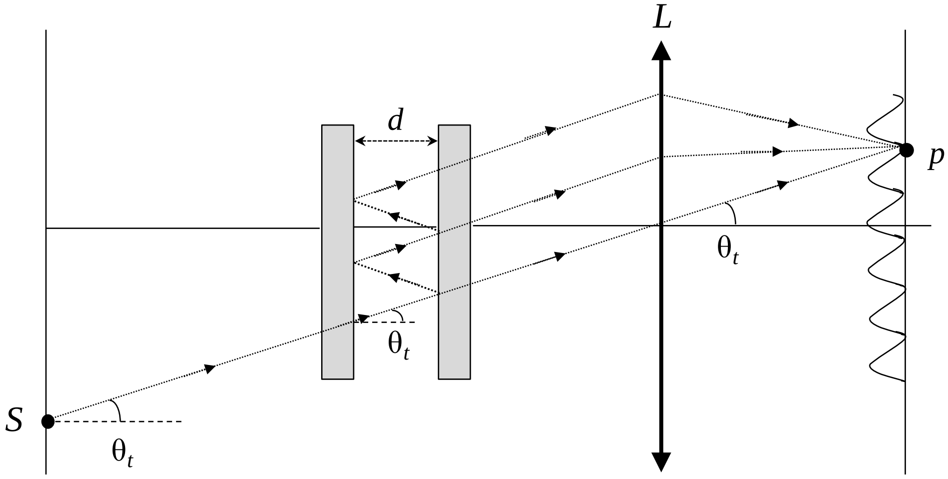

Figure 2.1 Fabry-Perot interferometer

Consider a narrow, monochromatic beam from an extended source point (*S*). This beam forms an angle (in the air) of θ_t with respect to the optical axis of the system, as in

Fig. 2.1. This single beam produces multiple coherent beams in the interferometer. The emerging set of parallel rays is brought together at point P in the focal plane of the converging lens (L). The nature of the superposition at P is determined by the path difference between successive parallel beams, $\Delta = 2n_f d cos\theta_t$. Using $n_f = 1$ for air, the condition for brightness is

$$2dcos\theta_t = m\lambda \tag{1}$$

Other beams from different source points, in the same plane, making the same angle θ_t with the axis satisfy the same path difference and arrive also at *P*. Eq. (1) satisfies for certain angles θ_t at fixed *d*. The fringe system is comprised of familiar concentric rings due to the focusing of fringes with equal inclination.

It is assumed that the two mirrors forming the Fabry-Perot cavity are identical. They are separated by a distance d and have real electric-field reflection; their transmission coefficients are *r* and *t*. Further, it is assumed that an electric field suffers no absorption upon encountering the cavity mirrors, so that

$$r^2 + t^2 = 1 \qquad \textit{Lossless mirrors} \tag{2}$$

A useful parameter associated with the FPI is the cavity round-trip time τ. This time is the time needed for light to circulate once around the cavity; it is given by

$$\tau = 2d/v = 2nd/c \tag{3}$$

where $v = c/n$ is the speed of light in the medium filling the space between the mirrors, *n* is the index of refraction of this medium, and c is the speed of light in a vacuum.

The electric field (E_T) transmitted through FPI can be calculated in terms of the field E_I incident on the interferometer, the reflection coefficient (r) of the cavity mirrors, and the length (*d*) of the cavity. In the following analysis, a propagation factor $P_F(\Delta z, \Delta t)$ is defined as the ratio of an electric field $E\ (z,\ t)$ associated with a traveling, monochromatic plane wave between position $z = z_0$ and $z = z_0 + \Delta z$ and between time $t = t_0$ and $t = t_0 + \Delta t$.

$$P_F(\Delta z, \Delta t) = E(z_0 + \Delta z, t_0 + \Delta t)/E(z_0, t_0) \qquad (4)$$

For a plane monochromatic wave that is moving z^+ direction,

$$P_F(\Delta z, \Delta t) = E_0 e^{i[\omega(t_0+\Delta t)-k(z_0+\Delta z)]}/E_0 e^{i(\omega t_0 - k z_0)} = e^{i(\omega\Delta t - k\Delta z)} \qquad (5)$$

The electric field moving toward the right in the cavity ($E_1{}^+$) is defined, so that $E_1{}^+$at the location of the first mirror should be

$$E_1^+ = E_{01}^+(t)e^{i\omega t} \qquad (6)$$

The incident electric field then becomes

$$E_I = E_{0I}(t)e^{i\omega t} \qquad (7)$$

At time $t + \tau$, when the electric field reflects once from the second mirror and returns back to the first mirror, the electric field $\mathrm{E}_1^+(t+\tau)$, moving toward the right, can be resolved as two parts. One part is the incident electric field $tE_I(t+\tau)$. This field is transmitted through the first mirror at this time. Another part is the total electric field $(r^2 P_F(\Delta z = 2d, \Delta t = \tau)\mathrm{E}_1^+(t))$ moving toward the right. This field exists at the first mirror before time τ that

$$E_1^+(t+\tau) = tE_I(t+\tau) + r^2 P_F(\Delta z = 2d, \Delta t = \tau)E_1^+(t) \qquad (8)$$

Equations (6) - (8) produce (9).

$$E_{01}^{+}(t+\tau)e^{i\omega(t+\tau)} = tE_{0I}e^{i\omega(t+\tau)} + r^2E_{01}^{+}(t)e^{i\omega t}e^{i(\omega\tau-2kd)} \tag{9}$$

If the electric field moving toward the right settles down into a steady-state when the incident electric field is first directed onto the cavity, $E_{01}^{+}(t+\tau) = E_{01}^{+}(t) = E_{01}^{+}$. Equation (10) can then be expressed as

$$E_{01}^{+} = tE_{0I}/(1-r^2e^{-i\delta}) \tag{10}$$

where $\delta = 2kd$ is the phase shift of the round trip.

The transmitted electric field E_T can be resolved through E_1^{+}propagating out of the second mirror.

$$\begin{aligned} E_T\left(t+\frac{\tau}{2}\right) = E_{0T}e^{i\omega(t+\tau/2)} = tP_F\left(\Delta z = d, \Delta t = \frac{\tau}{2}\right)E_1^{+}(t) \\ = r^2E_{01}^{+}(t)e^{i\omega t}e^{i(\omega\tau/2-\delta/2)} \end{aligned} \tag{11}$$

Adding Eq. (10) into (11) produces

$$E_{0T} = t^2E_{0I}e^{-i\delta/2}/(1-r^2e^{-i\delta}) \tag{12}$$

Here, the irradiation I_T is proportional to the product of E_{0T} and E_{0T}^{*}. Thus, the transmittance (T) of the FPI

$$\begin{aligned} T \equiv \frac{I_T}{I} = \frac{E_{0T}E_{0T}^{*}}{E_{0I}E_{0I}^{*}} = \frac{t^4E_{0I}e^{-\frac{i\delta}{2}}e^{\frac{i\delta}{2}}}{(1-r^2e^{-i\delta})(1-r^2e^{+i\delta})} \\ = \frac{t^4}{1+r^4-2r^2cos\delta} \end{aligned} \tag{13}$$

Equation (13), with Eq. (2), equals$(1-r^2)^2/(1+r^4-2r^2cos\delta)$ with $cos\delta = 1-2sin^2(\delta/2)$. Combining the two equations produces

$$T = \frac{1}{1 + [4r^2/(1-r^2)^2 sin^2(\delta/2)]} \tag{14}$$

Wherein $4r^2/(1-r^2)^2$ is defined as the coefficient of finesse (F).

Thus, Eq. (14) can be expressed as

$$T = \frac{1}{1 + F sin^2(\delta/2)} \tag{15}$$

Equations (14) and (15) suggest the transmittance (T) is related only to both the reflection coefficient (r) (or the finesse coefficient F) and the round trip phase shift (δ). Because the reflection coefficient r varies from 0 to 1, the finesse coefficient F (as the function of r) varies from 0 to infinity. For certain fixed value r, $T = T_{max} = 1$ at $\delta = m(2\pi)$, and $T = T_{min} = 1/(1+F)$ at $\delta = (m+1/2)2\pi$, where m is any integer. For the lossless mirrors, T_{max} always equals 1, regardless of the value of r, and T_{min}approaches zero while r approaches 1.

The reflectance (R) can be obtained in a manner similar to the transmittance (T):

$$\begin{aligned} R \equiv \frac{I_R}{I} = \frac{2r^2(1-cos\delta)}{1 + r^4 - 2r^2 cos\delta} \\ = \frac{4r^2/(1-r^2)^2 sin^2(\delta/2)}{1 + [4r^2/(1-r^2)^2 sin^2(\delta/2)]} \\ = \frac{1}{1 + 1/[F sin^2(\delta/2)]} \end{aligned} \tag{16}$$

When the r value is fixed, $R = R_{max} = 1$ at $\delta = m(2\pi)$ and $R = R_{min} = 1/(1 + 1/F)$ at $\delta = (m+1/2)2\pi$, where m is any integer.

Figure 2.2 illustrates the transmittance (T) versus the round-trip phase difference (δ) for selected values of the reflection coefficient r.

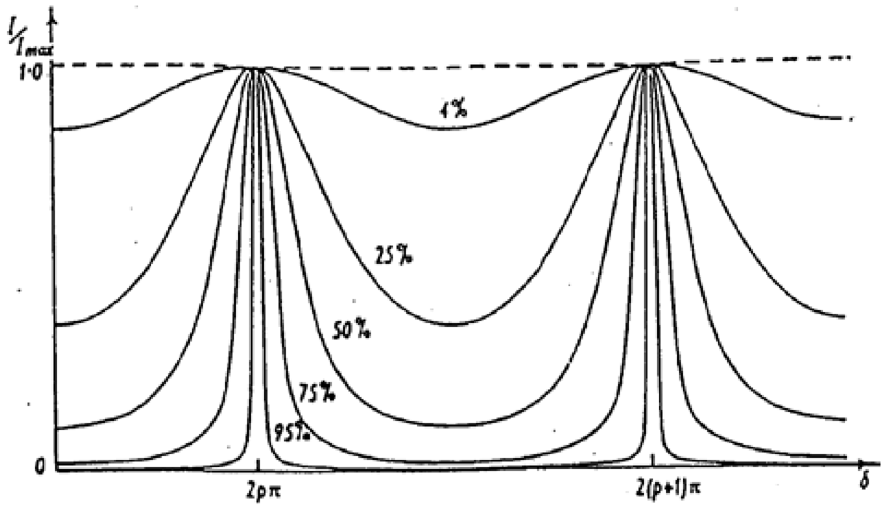

Figure 2.2 Reflectance ***R*** of FPI as a function of the round-trip phase difference **δ** for the increasing reflection coefficient ***r***

The quality of the cavity mirrors in FPI is measured in terms of the finesse coefficient F. The transmittance peaks sharply at higher values of r as the phase difference approaches integral multiples of 2π. it remains near zero for most of the region between fringes. In Fig. 2.2, the 95% reflectivity curve has the highest finesse; 4% has the least.

2.2. OPTICAL FIBER-BASED LOW FINESSE EXTRINSIC FABRY-PEROT INTERFEROMETER (EFPI)

In this thesis, the optical fiber-based Extrinsic Fabry-Perot Interferometer (EFPI) was used to demonstrate the microwave-assisted reconstruction of an optical interferogram for a distributed sensing concept[30, 32]. The reflectivity (R) used 4% because

$$R = (n_{fiber} - n_{air})/(n_{fiber} + n_{air}) \tag{17}$$

where n_{fiber} and n_{air} are the refractive index of fiber and air, respectively. An EFPI consists of two single-mode fiber spliced alignments with one segment of glass tube approximately 100um in length between them (see Fig. 2.3).

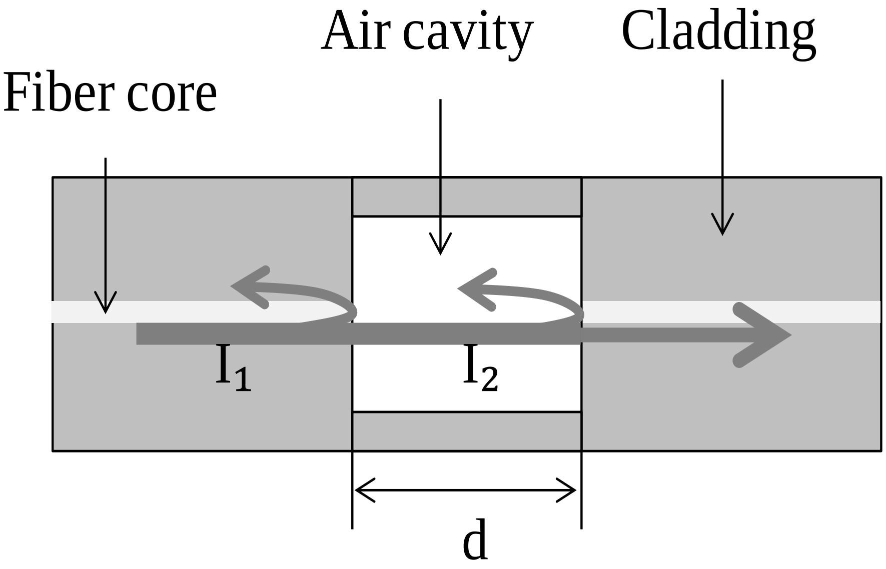

Figure 2.3 Schematic of the EFPI

The key principle of the optical fiber-based EFPI is the interference of two light waves. When the light wave reaches the first fiber/air interface, part of the light is reflected back the other propagates through the air cavity and reflected back on the second air/fiber interface. The two reflected light waves interfere with each other. Thus, the irradiance of the combined signals should be

$$I = I_1 + I_2 + 2\sqrt{I_1 I_2} cos\delta \tag{18}$$

where I_1 and I_2 are the reflections of the first and the second cavity interface, respectively, and δ is the total phase difference at the location of the recombined signals, as defined by

$$\delta = 4\pi nd/\lambda + \varphi_0 \tag{19}$$

where d is the cavity length, n is the refraction index of the cavity material (in this instance it is the refraction index of air), and $\varphi_0$is the initial phase.

The value of $cos\delta$ will determine the production of two interfered signals, either constructive or destructive interference. When $\delta = 2m\pi$ (m is any integer) and $cos\delta = +1$, the constructive interference generates maximum irradiance:

$$I = I_1 + I_2 + 2\sqrt{I_1 I_2} \tag{20}$$

When $\delta = (2m + 1)\pi$ and $cos\delta = -1$, the destructive interference generates minimum irradiance:

$$I = I_1 + I_2 - 2\sqrt{I_1 I_2} \tag{21}$$

For either two adjacent or successive minima,

$$\Delta\varphi = 4\pi d_1/\lambda_1 - 4\pi d_2/\lambda_2 = 2\pi, \;\; (n = 1 \; for\, air) \tag{22}$$

Using absolute cavity length d,

$$4\pi d = \frac{1}{\lambda_1} - \frac{1}{\lambda_2} = 2\pi \tag{23}$$

Thus, d can be resolved as

$$d = \frac{1}{2}(\frac{\lambda_1 \lambda_2}{\lambda_2 - \lambda_1}) \tag{24}$$

2.3. SENSING MECHANISM OF OPTICAL FIBER-BASED EFPI

2.3.1. Strain Sensing Mechanism of EFPI. When axial strain $\boldsymbol{\varepsilon}$ is applied to an EFPI, the cavity length ($\mathbf{d}$) will change. When the minimum irradiance caused by destructive interference is tracked, the resonance frequency will change, and, thus, the corresponding $\boldsymbol{\lambda}$ will change[33]. For destructive interference,

$$\delta = (2m + 1)\pi = 4\pi nd/\lambda + \varphi_0 \tag{25}$$

Equation (25) reveals that $\lambda = 4nd/[(2m + 1) - \varphi_0]$ and

$$\Delta\lambda = \frac{\lambda}{d}\Delta d \tag{26}$$

where $\Delta\lambda$ is the wavelength shift and Δd is the length difference of the cavity. Strain ε is defined as $\varepsilon = \Delta d/d$, the wavelength shift within the spectrum of an EFPI applied series strain can be considered a function of the strain ε:

$$\Delta\lambda = \varepsilon\,\lambda \tag{27}$$

Equation (27) reveals that the wavelength shift $\Delta\lambda$ will be different for different wavelengths (λ).

2.3.2. EFPI's Temperature Sensing Mechanism. When different temperatures are applied to an EFPI, the cavity length ($\mathbf{d}$) will change as both the sensor's glass components and the sealed air within the EFPI cavity expand thermally[34]. The wavelength shift $\Delta\boldsymbol{\lambda}$ can be derived from Eqs. (25) and (26):

$$\Delta\lambda = A\Delta T \tag{28}$$

where ΔT is the temperature difference applied on EFPI and A is the thermal coefficient related to EFPI property.

2.4. CONCEPT OF MICROWAVE-ASSISTED RECONSTRUCTION OF OPTICAL INTERFEROGRAMS

A low coherence light source (broadband source) is used as a carrier wave, and is intensity-modulated by a microwave signal. The intensity of the microwave modulated light can be expressed as:

$$I = I_0[1 + M \cdot cos(\omega t)] \tag{29}$$

where I_0 is the intensity of the light source, M is the modulation depth, and ω is the frequency of the microwave signal.

The microwave-modulated light is sent into an optical fiber with cascaded reflective EFPI sensors, so that the optical interference signal Γ_j of the j-th EFPI can be written as:

$$\Gamma_j = I_0[1 + M \cdot cos(\omega(t + \tau_j))] \cdot R_j \tag{30}$$

and

$$R_j(\lambda_m) = R_{j1} + R_{j2} + 2\sqrt{R_{j1}R_{j2}}cos(\frac{2\pi}{\lambda_m} \cdot OPD_j + \phi_j) \tag{31}$$

where Rj(λm) is the optical interference signal; Rj1 and Rj2 are the optical reflectivity of the two endfaces of the cavity, respectively; λm is the optical wavelength set by the optical tunable filter; OPDj is the optical path difference; ϕj is the initial phase; τj is the propagation delay of the microwave envelope of the j-th EFPI, which can be calculated using the following equation,

$$\tau_j = \frac{2D_j}{v} \tag{32}$$

where Dj is approximately the distance between the j-th sensor and the photodetector (PD), v is the group velocity of the microwave-modulated light transmitted inside the optical fiber.

The optical interference signals of the sensors travel backwards, and are detected by a high-speed photodetector. The optical signal is the superposition of all the cascaded EFPIs, given by,

$$Y = \sum_{j=1}^{N} \Gamma_j = \sum_{j=1}^{N} I_0 R_j \left[1 + M \cos\left(\omega (t + \tau_j) \right) \right] \tag{33}$$

where N is the total number of EFPIs cascaded along the fiber.

The optical detection is synchronized with the microwave modulation frequency (ω) so that the amplitude and the phase of the AC term (i.e., the cos(ωt) term in Eq. 5) are obtained. After scanning the microwave frequency through the entire available range, the complex microwave reflection spectrum (with both amplitude and phase) is obtained. By applying a complex and inverse Fourier-transform to the microwave spectrum, a series of delta functions are obtained at discrete time positions, given by:

$$y_j = AMI_0 R_j \quad at \quad t = \tau_j \text{ and } j = 1, 2, \ldots N \tag{34}$$

where A is the gain of the microwave detection.

As indicated in Eq. 34, the discrete time domain signals are proportional to the optical interference signals (R_j) of the cascaded EFPI sensors at a particular optical wavelength (λ_m) determined by the tunable filter. In addition, Eq. 34 also provides the locations of the sensors along the optical fiber because it has nonzero values only at the specific propagation delays (τ_j) corresponding to the sensor locations (D_j) as given by Eq. 32.

By sweeping the optical wavelength and repeating the microwave measurement, we can obtain the discrete optical interference signals (separated in the time domain) at different wavelengths. These data points can then be used to construct the optical interferograms of the cascaded EFPI sensors.

3. SYSTEM IMPLEMENTATION AND OPTIMIZATION

3.1. OPTIMIZE THE INTERROGATION SYSTEM

The modulation depth (or modulation index) of a modulation scheme is described by how much the modulated variable of the carrier signal varies around its unmodulated level. The modulation depth is defined differently in each modulation scheme. Modulation depth includes amplitude modulation depth, frequency modulation depth, and phase modulation depth. In this study, amplitude modulation depth was investigated because it formed the basis for the electro-optic modulator (EOM) [35].

AM modulation depth is the measure of the amplitude variation surrounding an un-modulated carrier. It indicates how much the modulation varies around its original level. Variations in the carrier amplitude (the AM) are defined as

$$MD = \frac{A - B}{A + B} \times 100\% \tag{35}$$

where A and B are the maximum and minimum peak-to-peak amplitudes of the modulated signal, respectively. The modulation depth must not exceed 100 percent to prevent the modulated spectrum becoming distorted.

3.1.1. EOM-based Amplitude Modulation. A Lucent 2623CS electro-optic modulator (EOM) (a Lithium Niobate modulator) was used in the experiment (see Fig. 3.1). This modulator had two FC/PC optical connectors. One connector served as an input for the original light signal. The other served as the output for the modulated light signal. It also included an SMA coaxial connector to input the RF message signal.

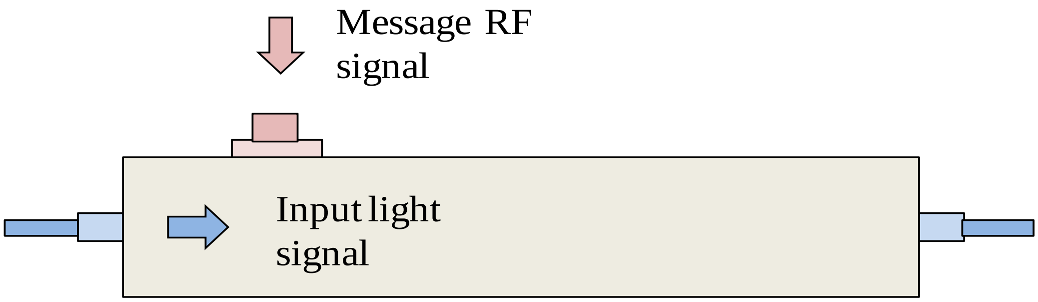

Figure 3.1 EOM schematic

DC bias voltage is an important parameter that must be considered when measuring an EOM’s AM modulation. Figure 3.2 illustrates the optical power out (dB) versus the modulator DC bias voltage (V) of an EOM.

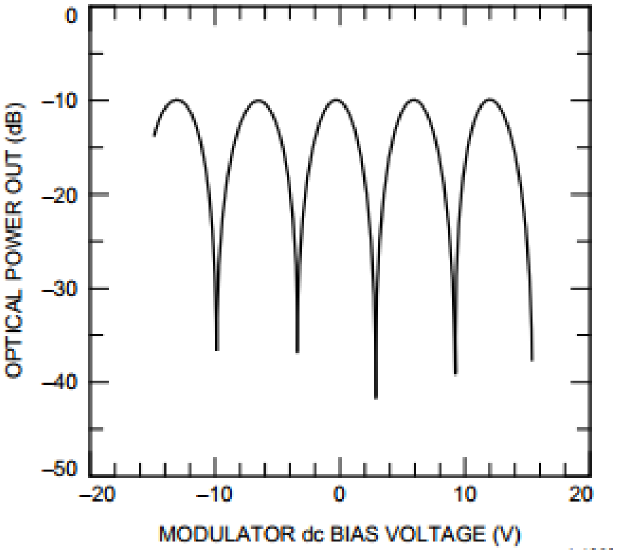

Figure 3.2 Optical power out (dB) versus modulator DC bias voltage (V)

The largest DC bias voltage value is not exactly zero; it is approximately -1.6V. A bias-tee must be used before the message RF signal input to give a DC bias voltage and realize the EOM to the largest optical power output.

3.1.2. Adjust the Input Polarization State to Optimize the Modulation Depth.

The polarization of the input carrier light signal is another important parameter when maximizing an EOM’s AM modulation depth. Panda-type polarization-maintaining fiber (PMF) is used as the optical input and output fiber with FC-type connectors[36] to polarize the light signal.

As an electromagnetic wave, light exhibits polarization. Polarization is a property of waves that can oscillate with more than one orientation. In general, the polarization of light is described by specifying the orientation of the wave's electric field at a point in space over one period of the oscillation. When light travels in free space, it propagates as a transverse wave. Polarization is perpendicular to the direction of propagation. However, in an optical fiber, polarization can be more complicated. Electromagnetic fields can have both longitudinal and transverse components such that EM waves are either TM or hybrid modes.

A polarizer is a device that can affect polarization (see Fig. 3.3). It serves as an optical filter that allows only light with a specific polarization to pass. It can switch a beam of either undefined light or mixed polarization light into a beam with well-defined polarization. Thus, the light sent by a broadband source can be polarized.

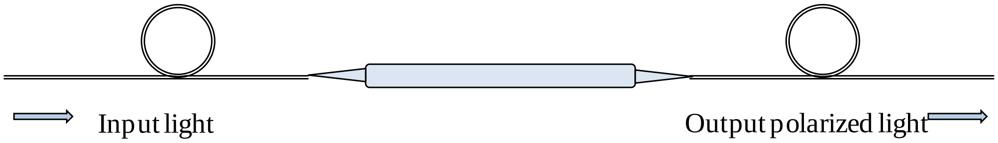

Figure 3.3 Schematic of a fiber in-line polarizer

Polarized light can be modified by a polarization controller. The polarization controller used in this study was a three-cascaded-rotatable-waveplate polarization controller (see Fig. 3.4).

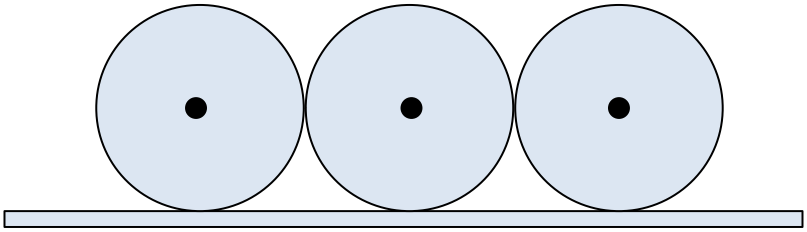

Figure 3.4 Schematic of a three waveplates polarization controller

The polarization controller utilizes stress induced birefringence to create three independent fractional wave plates. These wave plates alter the polarization in a single mode fiber. A single mode fiber is looped into three independent spools, creating three independent, fractional wave plates. The amount of birefringence induced in the fiber is a function of the fiber cladding diameter, the spool diameter (fixed), the number of fiber loops per spool, and the wavelength of the light. The fast axis of the fiber (in the spool's plane), is adjusted with respect to the transmitted polarization vector by manually rotating the paddles. A combination of three paddles (a quarter wave plate, a half wave plate, and a quarter wave plate) would be the necessary configuration to transform an arbitrary input polarization state into an arbitrary output polarization state. The first quarter wave plate would transform the input polarization state into a linear polarization state. The half wave plate would rotate the linear polarization state, and the last quarter wave plate would transform the linear state into an arbitrary polarization state. Therefore, adjusting each of the three paddles allows for complete control of the output polarization state.

An oscilloscope was used to detect the modulated signal's waveform and thus examine the AM modulation depth of the interrogation system. A schematic of the modulation depth detection experiment arrangement is illustrated in Fig. 3.5.

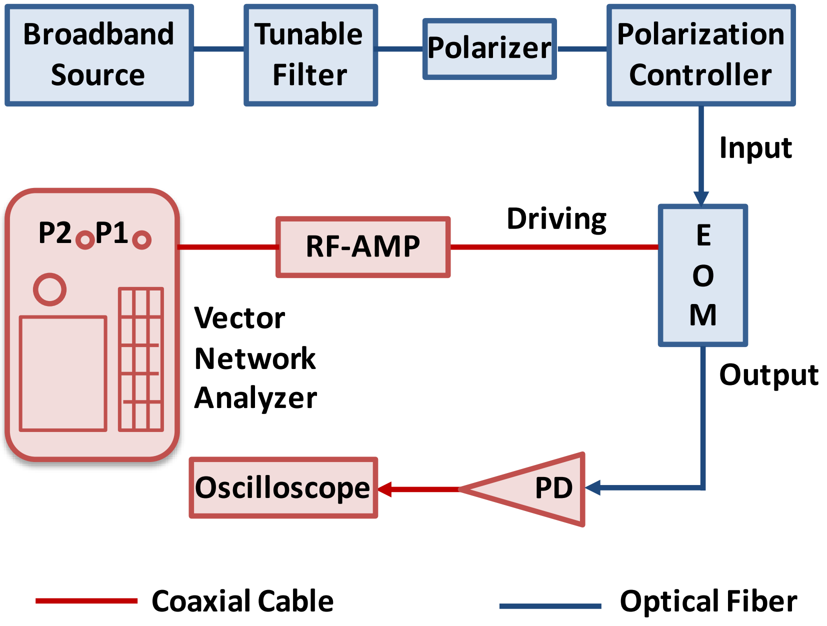

Figure 3.5 Schematic of the modulation depth arrangement

The light from a low coherence light source (broadband source) was launched into a tunable filter and then amplitude-modulated by a microwave signal through an electro-optic modulator. The full width at half maxima (FWHF) of the output profile for the tunable filter was approximately 1nm. The tunable filter's wavelength was set to 1550nm. An optical polarizer and an optical polarization controller are placed before the EOM to enhance the modulation efficiency or modulation depth. The port 1 of a VNA (e.g., HP 8753es) is used as the microwave message source. The modulation frequency of the microwave signal is set to 1GHz. The power of driving source was set to -11 dBm and then pre-amplified to 27 dBm. The microwave-modulated light (where the optical is the carrier and the microwave is the envelope) was then detected by a high-speed photodetector (PD), and the optic-electrical converted signal was sent into an oscilloscope. The peak to peak value was 1.6v. The waveform is illustrated in Fig. 3.6.

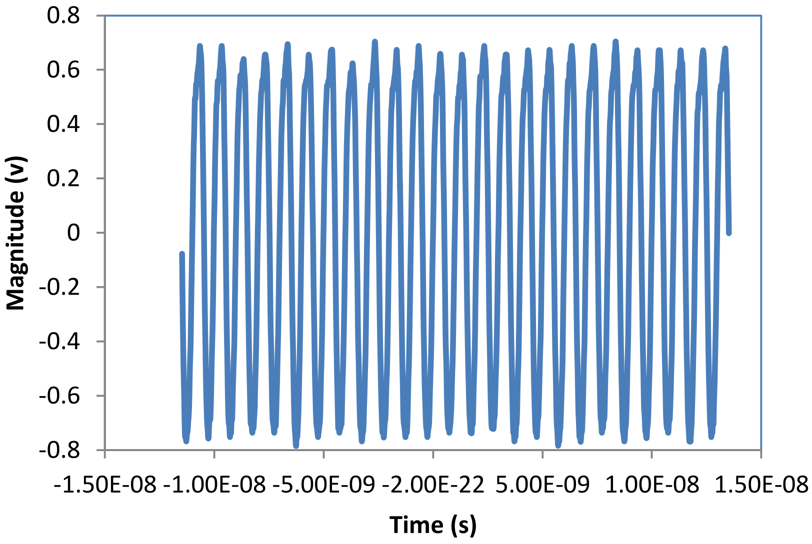

Figure 3.6 A modulation depth waveform as detected by an oscilloscope

3.2. CONTROL OF THE COHERENT LENGTH IN BOTH AN OPTICAL AND A MICROWAVE DOMAIN USED TO REALIZE LIGHT SIGNAL'S DISTRIBUTED CAPABILITY

3.2.1. Introduction of Coherence Length. Coherence is the correlation between phases of monochromatic radiations. In general, incoherence beams are with random phase relationships. In contrast, coherence beams are with a constant phase relationship. Coherence length is the propagation distance from a coherent source to a point where an electromagnetic wave maintains a specified degree of coherence[37]. For example, assume the source emits waves with wavelength $\lambda \pm \Delta\lambda$. Waves with wavelength λ and $\lambda + \Delta\lambda$ (which will constructively interfere in space) will destructively interfere after some optical path length Lc (the coherence length).

In radio-band systems, coherence length L is approximated by

$$L = \frac{c}{n\Delta f} \qquad (36)$$

Where c is the speed of light in a vacuum, n is the refractive index of the medium, and Δf is the bandwidth of the source.

In optical communications, coherence length L is given by

$$L = \frac{2\ln 2}{\pi n} \times \frac{\lambda^2}{\Delta\lambda} \qquad (37)$$

where λ is the central wavelength of the source, n is the refractive index of the medium, and $\Delta\lambda$ is the spectral width of the source.

3.2.2. Maximize the Microwave Coherence Length and Minimize the Optical Coherence Length. The key point of this approach involved utilizing a low coherence light source wherein the sensors would not coherently interfere with each other within the optical domain. In contrast, the microwave source needed to have a longer coherence length that would lead to coherence interference among the sensors. The phase information for each sensor could then be recorded, and the location information for each sensor could be resolved. Equations (36) and (37), indicate the bandwidth of source $\Delta \boldsymbol{f}$ was as small as possible. The spectral width $\Delta\boldsymbol{\lambda}$, however, was as large as possible.

3.3. VALIDATE THE INTERROGATION SYSTEM

3.3.1. System Realization. An experiment was performed to verify the proposed approach. Figure 3.7 is a schematic of the system's realization.

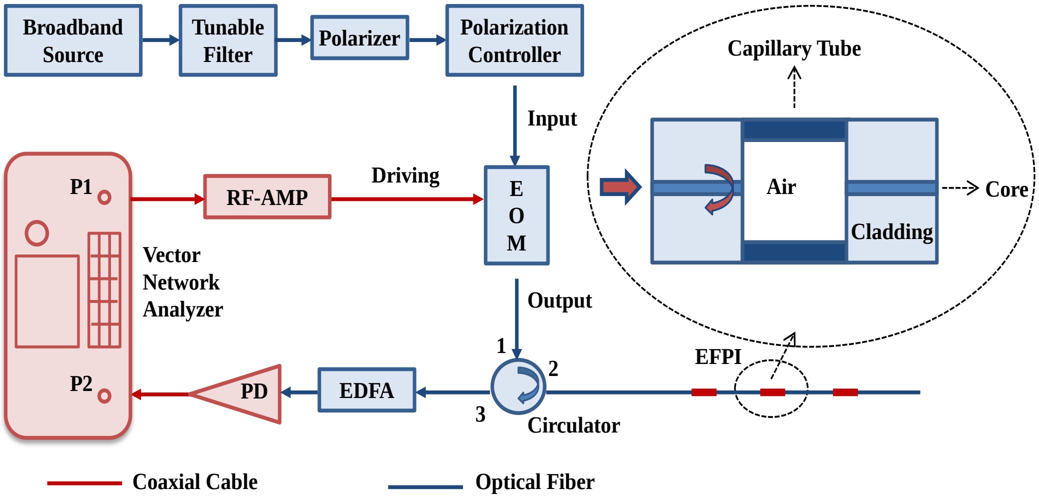

Figure 3.7 Schematic of an interrogation system for distributed fiber optic sensing. Acronyms used are defined as follows: RF-AMP is the radio frequency-amplifier. EOM is the electro-optic modulator. EDFA is the Erbium-doped fiber amplifier. PD is the photo-detector. EFPI is the extrinsic Fabry-Perot interferomter. P1/P2 is port 1/port 2

A broadband light source used was an amplified spontaneous emission (ASE) source emitting in the spectrum of 1530nm-1560nm. The light source was launched into a tunable filter and then amplitude modulated by a microwave signal through an electro-optic modulator. The full width at half maxima (FWHF) of the output profile for the tunable filter was approximately 1nm. This value corresponded with a coherence length of approximately 1 mm. Both an optical polarizer and an optical polarization controller were placed before the EOM to enhance either the modulation efficiency or modulation depth. Both the microwave source and the detector, including a PLL, were realized through a vector network analyzer (VNA, e.g., HP 8753es). The EOM was driven by port 1 of the VNA. A bias-tee was placed between the VNA and the EOM to give the microwave signal a DC bias voltage, allowing the amplitude modulation of the EOM can reach a higher value. The microwave source from port 1 was pre-amplified by an RF-amplifier to obtain the highest modulation index possible. So that by fine tuning the polarization controller and the driving power to the EOM, a modulation index of 100% at 3 GHz was obtained.

The modulated light was fed into an optical fiber with three cascaded extrinsic Fabry-Perot interferometers (EFPIs) via an optical circulator. The reflected signals from the three EFPIs were received by a high speed photo-detector that converted the light signal into a microwave analog signal. Each EFPI consisted of a capillary tube spliced into a single mode fiber at both ends with a certain cavity length. An Erbium-doped fiber amplifier (EDFA) was inserted between the photo-detector and the circulator, and Port 2 of the VNA was connected to the photo-detector.

Both the amplitude and the phase information from the reflected microwave spectrum were recorded by sweeping the VNA’s modulation frequencies. The recorded signal (scattering parameter S_{21} of the VNA) was then inverse Fourier-transformed to the time domain. Three reflections were observed in the time domain signal at a discrete location that corresponded with the reflections from three EFPIs.

The maximum amplitude of each reflection represents the response of each EFPI at that particular optical wavelength. The optical wavelength was swept to record the response of each sensor at different optical wavelengths. The interferogram of each EFPI within the optical spectrum domain could then be reconstructed simultaneously.

Figure 3.8 (a) and (b) are the two points of view of the experiment’s setup.

(a) (b)

Figure 3.8 Two points of view of the experiment arrangement

Three EFPIs (100 µm, 120 µm, and 130 µm) were cascaded through fusion splicing approximately 100 mm apart along a single mode fiber. The tunable filter was initially set at a center frequency of 1545 nm. The VNA’s intermediate frequency bandwidth (IFBW) was set to 300 Hz. The driving source’s power was set to -11 dBm at port 1 of VNA from 100 MHz to 6 GHz and then pre-amplified to 27 dBm for all frequency range to drive the EOM.

The microwave frequency was scanned at 1601 sampling points, from 100 MHz to 6 GHz. Both the amplitude and the phase information from port 2 were also recorded. This combined data revealed the microwave reflection spectrum (S_{21}). The time-resolved discrete reflections were obtained after a complex inverse Fourier transform was performed. The reflection amplitude of each EFPI was recorded, and then the tunable filter was swept to another center wavelength. A new time-resolved reflection signal was again recorded with this same procedure. The optical wavelength was swept through tunable filter and the corresponding microwave signal was recorded. The optical interferogram of each EFPI with the in wavelength domain was then reconstructed simultaneously.

The whole procedure took about 1 minute, which included the time required for the VNA to scan through the entire available frequency span, data acquisition, signal analysis, stepping the wavelength of the tunable filter through the spectrum range, and interferogram reconstruction.

3.3.2. Design and Fabrication of Optical Fiber Based EFPI. Although simple in structure, FPI is a high-resolution instrument with a wide range of applications.

An FPI is typically comprised of two parallel, highly reflective mirrors. These mirrors produce an interference pattern that results from a superposition of multiple beams from the transmitted light. FPIs are widely used in telecommunications, lasers, and spectroscopy control. They are also used for the precise measurement of a light’s wavelength. They help determine both the refractive indices of gasses as well as the calibration of the standard meter in terms of wavelengths.

Two types of FPI have been developed on fiber optic techniques including extrinsic Fabry-Perot interferometer (EFPI) and intrinsic Fabry-Perot interferometer (IFPI).

An EFPI uses an air cavity between two cleaved fiber ends. An IFPI uses the semi-reflecting surfaces created inside a fiber. Both EFPI and IFPI configurations hold advantages for single point and quasi-distributed applications, such as high environmental and mechanical stability, due to an all-silica design, a relatively high strain sensitivity, low temperature dependence, and low transmission loss. An EFPI consists of one segment of capillary tube (about 100um) splicing between two segments of standard single mode fiber (SMF) (see Fig. 2.3).

EFPI has been fabricated for quite some time through a technique reported as an in-line fiber etalon. In this study, standard Corning, SMF-28 single mode fiber was used for fabrication. Figure 3.9 illustrates the sensor after fabrication, as seen through a microscope. The outer diameter of the hollow tube used was equal to the outer diameter of the SMF-28. The tube’s wall thickness was 25 um. A cleaved-end section of SMF (lead-in fiber) was Arc-fused to the cleaved-end of the hollow silica tube. The polymer coated on the glass tube’s surface had to be removed to cleave silica tube to the hollow tube. The other end was then carefully cleaved at the desired length under a microscope. The microscope was attached to a moving stage with a high resolution digital scale to obtain a precise distance.

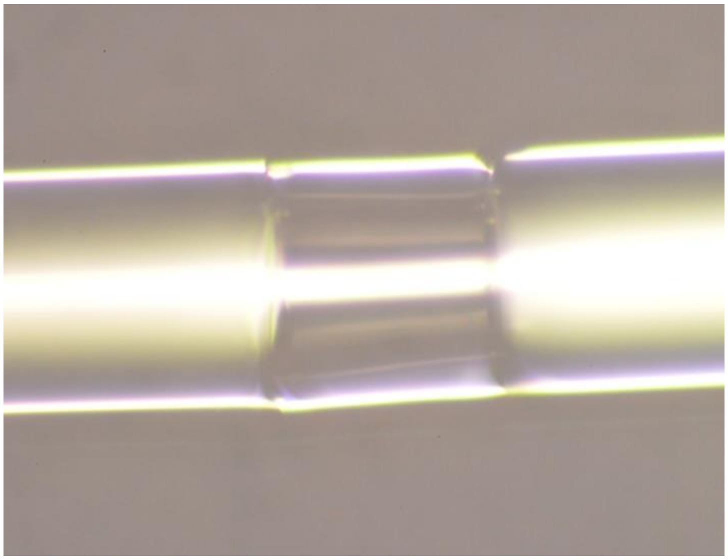

Figure 3.9 In-line EFPI sensor as seen through the microscope

An arc power of 19 W for 1.5 sec was utilized to fuse the single-mode fibers. The fusion of SMF to a hollow silica tube, however, required less arc-power (i.e., 7 W for 0.5 sec). After the glass tube was cleaved, the cleaved end of the tube was arc-fused with another (lead-out) SMF.

3.3.3. Reconstruction of Optical Interferograms Using Cascaded EFPIs. Figure 3.10 (a) illustrates the time-resolved discrete reflections at which the optical carrier wavelength is tuned to 1553 nm.

Three reflections (three EFPIs) appear within the time domain. Although the two air/glass interfaces in each capillary tube will induce two reflections, they cannot be resolved in microwave domain due to the wavelength of microwave is much larger comparing to the length of the tube. Essentially, only one reflection at the tube can be seen through microwave instruments. The distance between two consecutive EFPIs is far larger than the coherence length of the input light source so that no interference exists between any two EFPIs. Figure 3.10 illustrates a good SNR for each reflection peak. These amplitudes, however, decreased gradually due to not only a large reflectivity but also a transmission loss of the capillary tubes. The tunable filter was configured from 1545 nm to 1560 nm with a 1 nm sampling interval. The entire procedure took approximately 1 minute to complete. (This time includes the reconstruction of three optical interferograms.)

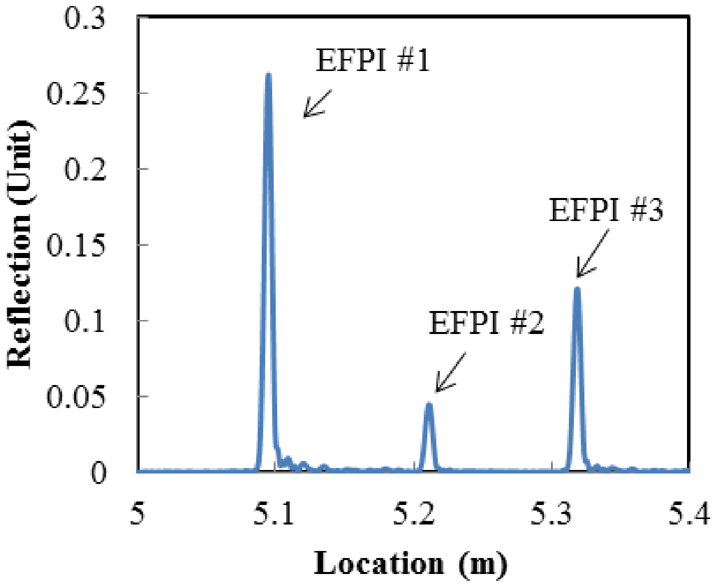

(a)

Figure 3.10 Time domain signal after applying a complex inverse Fourier transform to the microwave spectrum at 1553 nm, and microwave reconstructed optical interferogram of the EFPIs versus their spectra taken individually from the OSA, respectively

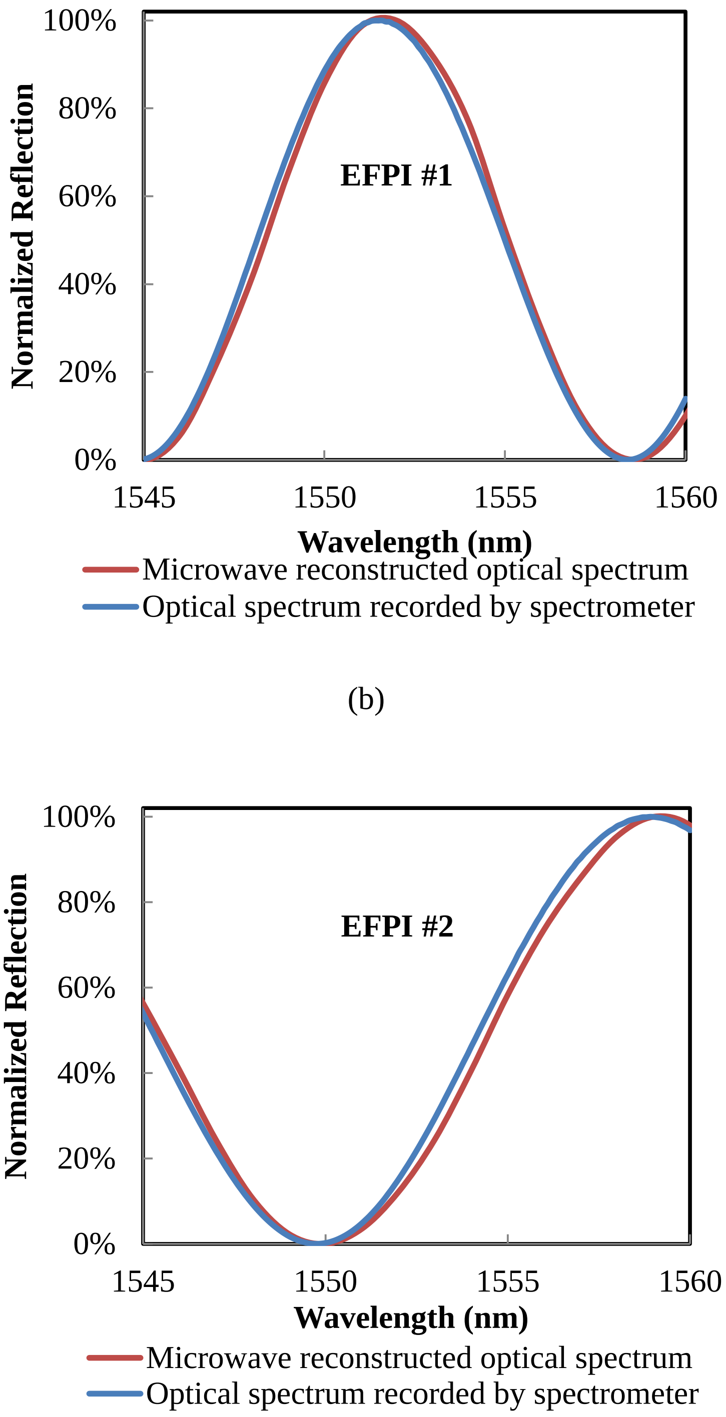

(b)

(c)

Figure 3.10 Time domain signal after applying a complex inverse Fourier transform to the microwave spectrum at 1553 nm, and microwave reconstructed optical interferogram of the EFPIs versus their spectra taken individually from the OSA, respectively (Cont.)

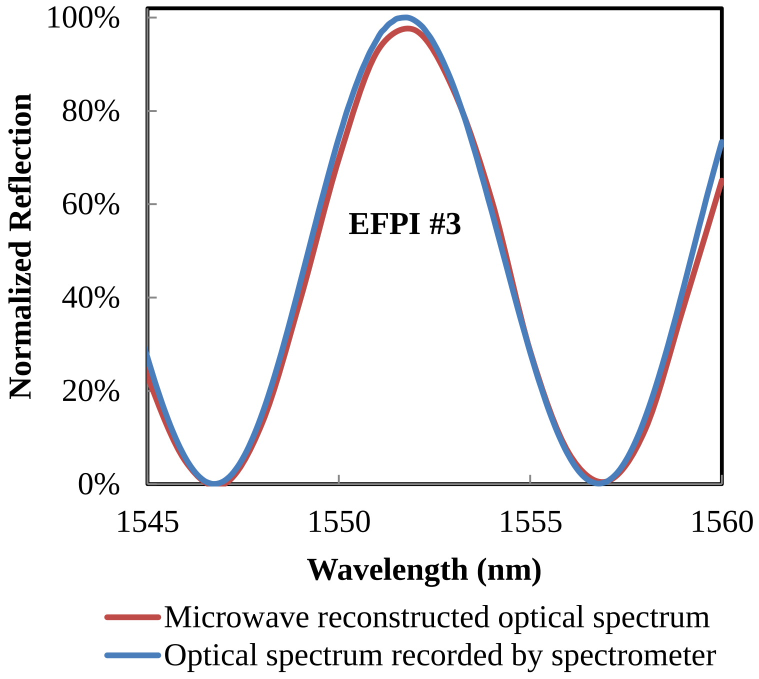

(d)

Figure 3.10 Time domain signal after applying a complex inverse Fourier transform to the microwave spectrum at 1553 nm, and microwave reconstructed optical interferogram of the EFPIs versus their spectra taken individually from the OSA, respectively (Cont.)

Figure 3.10 (b) (c) (d) illustrates the reconstructed optical interferogram of each EFPI, respectively. The red curve in each figure represents the microwave reconstructed optical interferogram. The blue curve represents the microwave reconstructed optical interferogram recorded individually through a conventional optical spectrum analyzer (OSA). All reflected intensities were normalized based on their corresponding optical intensities for comparison. It suggests that the microwave reconstructed optical interferogram match well with the interference patterns taken from the OSA. Some differences, or mismatches, however, exist in the compared spectra. These differences resulted from both the uneven gain coefficient within the entire band of the EDFA and the different sampling points between the microwave interrogation system and the OSA.

4. EXPERIMENTAL RESULTS

To prove the effectiveness of the proposed method for distributed sensing, a strain test was performed. The axial strain was applied to the second EFPI while the other two sensors stayed the same. Two ends of the second were tightly attached to a motorized translation stage and a fixed stage using all-purpose glue, respectively. The length between two attaching points, where the EFPI was in the center, was precisely controlled to 100 mm. The microwave reconstructed optical spectra of the three EFPIs were recorded as the distance between the two points was increased step by step. The strain was applied at a step of 5 μm, corresponding to 50 με for the total length of 100 mm.

By applying the 4th order polynomial curve-fitting to all the reconstructed spectra and monitoring the resonant frequency of each sensor, the wavelength shift of each sensor was plotted as a function of the axial strain. Figure 4.1 shows applied strain distribution along an optical fiber with three multiplexed EFPIs. The second sensor has an obvious response to the applied strain while the other sensors have no responses, indicating that the proposed distributed sensing method based on microwave reconstructed optical spectra has little crosstalk among sensors. Figure 4.2 plots the second sensor in response to the applied axial strain, where the wavelength shift of the interferogram is a linear function of the applied strain with a slope of 0.0024 nm/με. Figure 4.3 plots the shift in reconstructed spectra as the applied strain increased. The increasing strain did not incur any significant loss in the reflection spectra. The spectra of the other two sensors (which are not shown here) have no any observable shift. As such, the proposed method for distributed sensing based on optical fiber works well and can be designed for measurement of various physical, chemical and biological parameters.

Example applications include the monitoring of displacement, strain, pressure, acoustic/ultrasonic waves, refractive index, liquid level, gas or vapor concentration, biological quantity, etc.

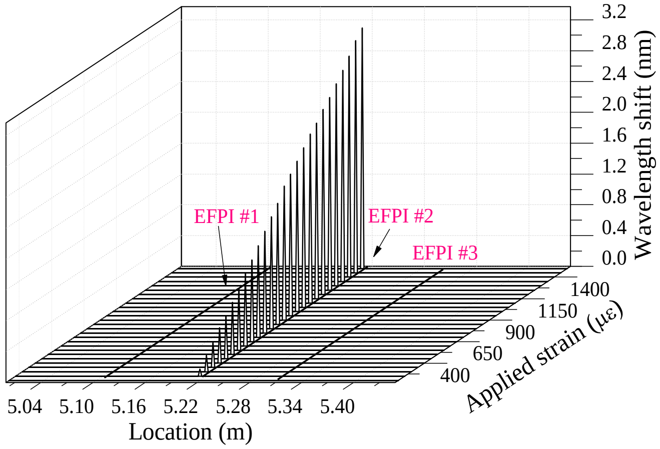

Figure 4.1 Strain distribution of an optical fiber with three multiplexed EFPI sensors

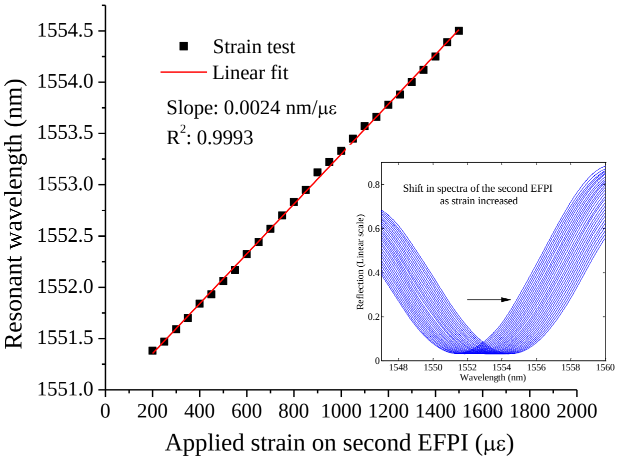

Figure 4.2 Resonant wavelength shift of the second EFPI sensor as a function of applied strain. Inset: Shift in spectra of the second EFPI as strain increased

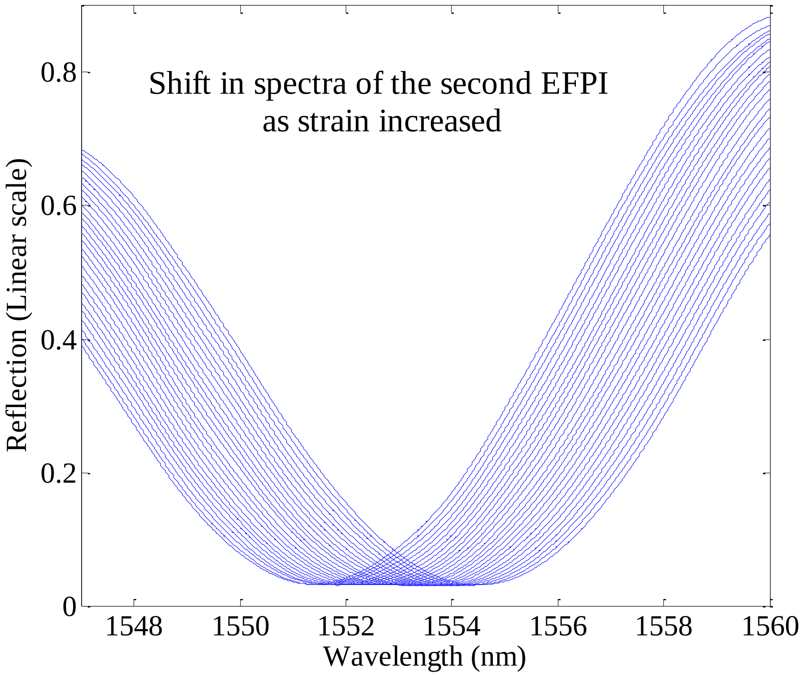

Figure 4.3 Shift in spectra of the second EFPI as strain increased

The spatial resolution ΔD_{min} (i.e., the minimum distance between two adjacent sensors) is determined by the microwave frequency bandwidth according to the following equation,

$$\Delta D_{\min} = \frac{1}{2B_{RF}} v \tag{38}$$

where B_{RF} is the bandwidth (i.e., the maximum scanning frequency range) of the microwave source. A larger bandwidth results in a better spatial resolution. For example, if the bandwidth of the microwave source is 6GHz, the minimum distance between two adjacent sensors is about 1.7cm. Of course as stated earlier, the separation between two sensors needs to be significantly larger than the coherence length of the spectrally filtered optical source to avoid the optical interference between two adjacent sensors.

Because the cascaded EFPIs are uniquely identified in the microwave domain, they can be made to have the same OPD. On contrast, the typical optical spectral domain Fourier transform based multiplexing method [38, 39] requires the multiplexed sensors to have significantly different OPDs. The maximum number of sensors can be multiplexed depends on the insertion loss (including reflection) of each sensor, the dynamic range of the microwave instrument, and the dynamic range of the photo-detector. In general, the cascaded EFPIs can be made to have weak reflectivity to reduce the insertion loss. The optical signals can be further amplified by using EDFAs. It is expected that the reported microwave method is able to multiplex much more interferometers than the typical optical spectral domain Fourier transform based multiplexing method.

5. CONCLUSIONS AND FUTURE WORK

5.1. CONCLUSIONS

To summarize, the microwave assisted reconstruction of optical interferograms for distributed fiber optics sensing concept is proposed in this thesis. The fundamental approach is to send the microwave-modulated optical signal through an optical fiber sensor network and the reflected signal is recorded in microwave domain. By properly controlling the coherence length of the optical input and sweeping its wavelength step by step, the reflection spectrum of each sensor along an optical fiber can be reconstructed. To optimize the interrogation system, the modulation depth of EOM is enhanced by applying a certain value of dc bias voltage to the modulation microwave signal, and by using a polarizer and a polarization controller to polarize the light source and to modify its polarization state. To avoid the coherent interference of each sensor in optical domain, and to clearly resolve the position information for each sensor in microwave domain, a low coherence light source and a high coherence microwave source are utilized. Three cascaded EFPIs along an optical fiber were used to demonstrate the concept. The optical interferogram in spectrum domain of each EFPI was reconstructed simultaneously and they matched well with the ones recorded individually from the optical spectrometer. It is demonstrated that the EFPI has low sensitivity to temperature, but high sensitivity to strain. Strain sensing was conducted to prove its effect in distributed sensing. It is necessary to note that although three EFPIs are used here for the purpose of demonstration of the concept, other forms of fiber optical sensors can also be implemented to reconstruct their optical spectra, and it is expected that the proposed distributed sensing technique has a large multiplexing capability while maintaining a high measurement resolution.

5.2. FUTURE WORK

- Utilize Intrinsic Febry-Perot Interferometer (IFPI) instead of EFPI, due to its weak reflectivity.

- Develop embedded sensors into components and structures for distributed health monitoring (e.g., crack, deflection, vibration and corrosion) in extreme environments.

BIBLIOGRAPHY

[1] S. Kim, S. Pakzad, D. Culler, J. Demmel, G. Fenves, S. Glaser, "Health monitoring of civil infrastructures using wireless sensor networks," presented at *the Proceedings of the 6th international conference on Information processing in sensor networks*, Cambridge, Massachusetts, USA, 2007.

[2] J. Leng and A. Asundi, "Structural health monitoring of smart composite materials by using EFPI and FBG sensors," *Sensors and Actuators A: Physical,* vol. 103, pp. 330-340, // 2003.

[3] J. Brownjohn, "Structural health monitoring of civil infrastructure," *Philosophical Transactions of the Royal Society A: Mathematical, Physical and Engineering Sciences,* vol. 365, pp. 589-622, 2007.

[4] C. R. Farrar and K. Worden, "An introduction to structural health monitoring," *Philosophical Transactions of the Royal Society A: Mathematical, Physical and Engineering Sciences,* vol. 365, pp. 303-315, 2007.

[5] A. Mehta, W. Mohammed, and E. G. Johnson, "Multimode interference-based fiber-optic displacement sensor," *Photonics Technology Letters, IEEE,* vol. 15, pp. 1129-1131, 2003.

[6] H.-N. Li, D.-S. Li, and G.-B. Song, "Recent applications of fiber optic sensors to health monitoring in civil engineering," *Engineering structures,* vol. 26, pp. 1647-1657, 2004.

[7] Y.-J. Rao, Y.-P. Wang, Z.-L. Ran, and T. Zhu, "Novel fiber-optic sensors based on long-period fiber gratings written by high-frequency CO_2 laser pulses," *Lightwave Technology, Journal of,* vol. 21, pp. 1320-1327, 2003.

[8] A. D. Kersey, M. A. Davis, H. J. Patrick, M. LeBlanc, K. Koo, C. Askins, "Fiber grating sensors," *Lightwave Technology, Journal of,* vol. 15, pp. 1442-1463, 1997.

[9] B. Lee, "Review of the present status of optical fiber sensors," *Optical Fiber Technology,* vol. 9, pp. 57-79, 2003.

[10] B. Spencer, M. E. Ruiz ‐ Sandoval, and N. Kurata, "Smart sensing technology: opportunities and challenges," *Structural Control and Health Monitoring,* vol. 11, pp. 349-368, 2004.

[11] S. Jang, H. Jo, S. Cho, K. Mechitov, J. A. Rice, S.-H. Sim, "Structural health monitoring of a cable-stayed bridge using smart sensor technology: deployment and evaluation," *Smart Structures and Systems,* vol. 6, pp. 439-459, 2010.

[12] J. A. Rice, K. Mechitov, S.-H. Sim, T. Nagayama, S. Jang, R. Kim, "Flexible smart sensor framework for autonomous structural health monitoring," *Smart Structures and Systems,* vol. 6, pp. 423-438, 2010.

[13] J. Li, T. Nagayama, K. A. Mechitov, and B. F. Spencer Jr, "Efficient campaign-type structural health monitoring using wireless smart sensors," in *SPIE Smart Structures and Materials+ Nondestructive Evaluation and Health Monitoring,* 2012, pp. 83450U-83450U-11.

[14] G. Zhou and L. Sim, "Damage detection and assessment in fibre-reinforced composite structures with embedded fibre optic sensors-review," *Smart Materials and Structures,* vol. 11, p. 925, 2002.

[15] J. S. S. M. S. Cusworth, "Multiplexing techniques for noninterferometric optical point-sensor networks: a review," *Fiber & Integrated Optics,* vol. 17, pp. 3-20, 1998.

[16] C. G. Askins, M. A. Putnam, and E. J. Friebele, "Instrumentation for interrogating many-element fiber Bragg grating arrays," in *Smart Structures & Materials' 95,* 1995, pp. 257-266.

[17] W. W. Morey, J. R. Dunphy, and G. Meltz, "Multiplexing fiber Bragg grating sensors," in *Distributed and Multiplexed Fiber Optic Sensors,* 1992, pp. 216-224.

[18] M. Majumder, T. K. Gangopadhyay, A. K. Chakraborty, K. Dasgupta, and D. K. Bhattacharya, "Fibre Bragg gratings in structural health monitoring—Present status and applications," *Sensors and Actuators A: Physical,* vol. 147, pp. 150-164, 2008.

[19] C. Rodrigues, C. Félix, A. Lage, and J. Figueiras, "Development of a long-term monitoring system based on FBG sensors applied to concrete bridges," *Engineering Structures,* vol. 32, pp. 1993-2002, 2010.

[20] Y. Wang, J. Gong, D. Y. Wang, B. Dong, W. Bi, and A. Wang, "A quasi-distributed sensing network with time-division-multiplexed fiber Bragg gratings," *Photonics Technology Letters, IEEE,* vol. 23, pp. 70-72, 2011.

[21] M. Zhang, Q. Sun, Z. Wang, X. Li, H. Liu, and D. Liu, "A large capacity sensing network with identical weak fiber Bragg gratings multiplexing," *Optics Communications,* vol. 285, pp. 3082-3087, 2012.

[22] A. J. Rogers, "Polarization-optical time domain reflectometry: A technique for the measurement of field distributions," *Applied Optics,* vol. 20, pp. 1060-1074, 1981.

[23] D. L. Philen, I. A. White, J. F. Kuhl, and S. C. Mettler, "Single-mode fiber OTDR: Experiment and theory," *Microwave Theory and Techniques, IEEE Transactions on,* vol. 30, pp. 1487-1496, 1982.

[24] Y. Dong, L. Chen, and X. Bao, "Time-division multiplexing-based BOTDA over 100km sensing length," *Optics Letters,* vol. 36, pp. 277-279, 2011.

[25] T. Chen, Q. Wang, R. Chen, B. Zhang, K. P. Chen, M. Maklad, "Distributed hydrogen sensing using in-fiber Rayleigh scattering," *Applied Physics Letters,* vol. 100, pp. 191105-191105-3, 2012.

[26] W. Eickhoff and R. Ulrich, "Optical frequency domain reflectometry in single‐mode fiber," *Applied Physics Letters,* vol. 39, pp. 693-695, 1981.

[27] B. J. Soller, D. K. Gifford, M. S. Wolfe, and M. E. Froggatt, "High resolution optical frequency domain reflectometry for characterization of components and assemblies," *Opt. Express,* vol. 13, pp. 666-674, 2005.

[28] R. Passy, N. Gisin, J.-P. von der Weid, and H. Gilgen, "Experimental and theoretical investigations of coherent OFDR with semiconductor laser sources," *Lightwave Technology, Journal of,* vol. 12, pp. 1622-1630, 1994.

[29] J. Vaughan, *The Fabry-Perot interferometer: history, theory, practice, and applications*: Taylor & Francis, 1989.

[30] B. E. Saleh, M. C. Teich, and B. E. Saleh, *Fundamentals of photonics* vol. 22: Wiley New York, 1991.

[31] S. Yin, P. B. Ruffin, and T. Francis, *Fiber optic sensors* vol. 132: CRC PressI Llc, 2008.

[32] J. Leng and A. Asundi, "Real-time cure monitoring of smart composite materials using extrinsic Fabry-Perot interferometer and fiber Bragg grating sensors," *Smart materials and structures,* vol. 11, p. 249, 2002.

[33] M. Schmidt, B. Werther, N. Fuerstenau, M. Matthias, and T. Melz, "Fiber-Optic Extrinsic Fabry-Perot Interferometer Strain Sensor with< 50 pm displacement resolution using three-wavelength digital phase demodulation," *Optics Express,* vol. 8, pp. 475-480, 2001.

[34] T. Wei, Y. Han, Y. Li, H.-L. Tsai, and H. Xiao, "Temperature-insensitive miniaturized fiber inline Fabry-Perot interferometer for highly sensitive refractive index measurement," *Opt. Express,* vol. 16, pp. 5764-5769, 2008.

[35] G. H. Wakefield and N. F. Viemeister, "Discrimination of modulation depth of sinusoidal amplitude modulation (SAM) noise," *The Journal of the Acoustical Society of America,* vol. 88, p. 1367, 1990.

[36] C. Zhang, B. Zhao, B. Xiangli, and X. Zha, "Analysis of the modulation depth affected by the polarization orientation in polarization interference imaging spectrometers," *Optics Communications,* vol. 227, pp. 221-225, 2003.

[37] C. Kittel and P. McEuen, *Introduction to solid state physics* vol. 7: Wiley New York, 1996.

[38] J. Wang, B. Dong, E. Lally, J. Gong, M. Han, and A. Wang, "Multiplexed high temperature sensing with sapphire fiber air gap-based extrinsic Fabry–Perot interferometers," *Opt. Letters 35,* 619-621 (2010).

[39] X. Li, Q. Sun, D. Liu, R. Liang, J. Zhang, J. Wo, P. P. Shum, and D. Liu, "Simultaneous wavelength and frequency encoded microstructure based quasi-distributed temperature sensor," *Opt. Express 20*, 12076-12084 (2012).

PAPER

CHARACTERIZATION OF PCB DIELECTRIC PROPERTIES USING TWO STRIPLINES ON THE SAME BOARD

ABSTRACT

Signal integrity (SI) and power integrity (PI) modelling and design require accurate knowledge of dielectric properties of printed circuit board (PCB) laminate dielectrics. Dielectric properties of a laminate dielectric can be obtained from a set of the measured S-parameters on a PCB stripline with a specially designed through-reflect-line (TRL) calibration pattern. In this work, it is proposed to extract dielectric properties from the measurements of S-parameters on the two 50-Ohm stripline structures of the same length, but different widths of the trace, designed on the same layer of a PCB. The dielectric properties on these two lines should be identical. However, an application of the simplest "root-omega" technique to extract dielectric properties of the substrate would lead to the ambiguity in the extracted data. This is because the conductor surface roughness affects the measured S-parameters and is lumped in the extracted dielectric data. This problem of ambiguity in the dielectric properties extraction can be overcome using the approach analogous to the recently proposed method to separate dielectric and conductor losses on PCB lines with different widths and roughness profiles [1].

1. INTRODUCTION

Building a wide-band model of a channel to understand its signal transmission characteristics is important for high-speed digital design. The accurate knowledge of the frequency-dependent dielectric properties of the printed circuit board (PCB) laminate dielectric over a wide frequency range is required for channel modeling [1]-[3] .

There are several methods available for determining the dielectric properties [2]-[5]. Each method has its own advantages and limitations. The “root-omega” method [3] uses the s-parameters of a single transmission line, to determine the dielectric constant. This method does not separate the conductor roughness effect from the dielectric loss. The conductors in the PCB are purposely made rough during manufacturing for adhesion purposes, but this conductor surface roughness introduces a loss which cannot be neglected at frequencies above a few gigahertzes [4]. From the signal integrity point of view, if roughness effects upon signal propagation on printed circuit boards are not taken into account or underestimated inaccuracy in the extracted dielectric properties may result in significant errors in simulation results [4]. A way to methodically remove the effect of the conductor roughness is shown in the [1], wherein the refined ambient effective dielectric properties are extracted using two approaches. The first approach requires at least three test vehicle with the same dielectric material and geometry, but different conductor surface roughness profiles. The second approach requires the test vehicles with the same dielectric material, almost the same roughness, but different geometry (width of the signal trace).

Herein, a method, which is the further development of the second approach described in [1], is used to extract the dielectric properties of PCB laminate dielectrics.

These dielectric properties are independent of the conductor roughness effects, and represent the ambient dielectric around the trace composed of glass fibers and resin. The composite fiber-glass filled laminate dielectric with the found effective dielectric properties refined from the conductor roughness effects will be further referred as the "refined ambient dielectric". In the proposed test vehicle design, there are two stripline traces with different widths. These are the narrow and wide traces routed in the same layer of the board. This means that both the conductor roughness of the traces and the ambient dielectric material are the same. The total attenuation constant α_T and the total phase constant β_T for both traces are calculated from the measured S-parameters. The port effects in the measurements of S-parameters are removed using the TRL calibration procedure on the specially designed TRL pattern [6]. The dielectric loss α_D and the dielectric phase constant β_D are extracted by taking advantage of the dependence of the components of attenuation constant on the dimensions of the trace and conductor roughness profiles, analogous to [1]. The cross-sectional analysis of PCB striplines is used for estimation of the stripline dimensions and roughness profiles on the sides of traces.

In Section 2, the thru-reflect-line (TRL) calibration method, the methodologies of dielectric properties extraction for root-omega method and the proposed new method, are introduced. Section 3 provides the results for the extraction of dielectric constant (Dk) and the dissipation factor (Df), comparing the two methods, and discusses some issues in measurements and future work.

2. METHODOLOGY

The methodology requires two striplines with traces of different widths, but the same laminate substrate and almost identical conductor roughness profiles. To achieve this, the traces, as shown in Fig. 1, are placed in the same layer of the PCB, ensuring practically the same roughness profiles of the traces. As the traces have different widths, to achieve the 50-Ω characteristic impedances, they are referenced to different planes. As a result, the wider trace has more dielectric layers between the trace and the reference plane than the narrow one. For the more accurate material characterization using transmission line methods, usually long traces are used. In this study, they are chosen 10 inches long. Then, to achieve immunity to any glass-weave effects on the long transmission lines, the angle of 10 °to the edge of the board is used, which is known to have the reduced glass weave effects[5].

Herein, the TRL calibration is used on each test line to remove the port effects on the S-parameters in the frequency range of concern. These port effects can be due to discontinuities or non-transmission line structures, like vias or connectors. Below the TRL calibration pattern is explained, followed by the methodology used for the material parameter extraction.

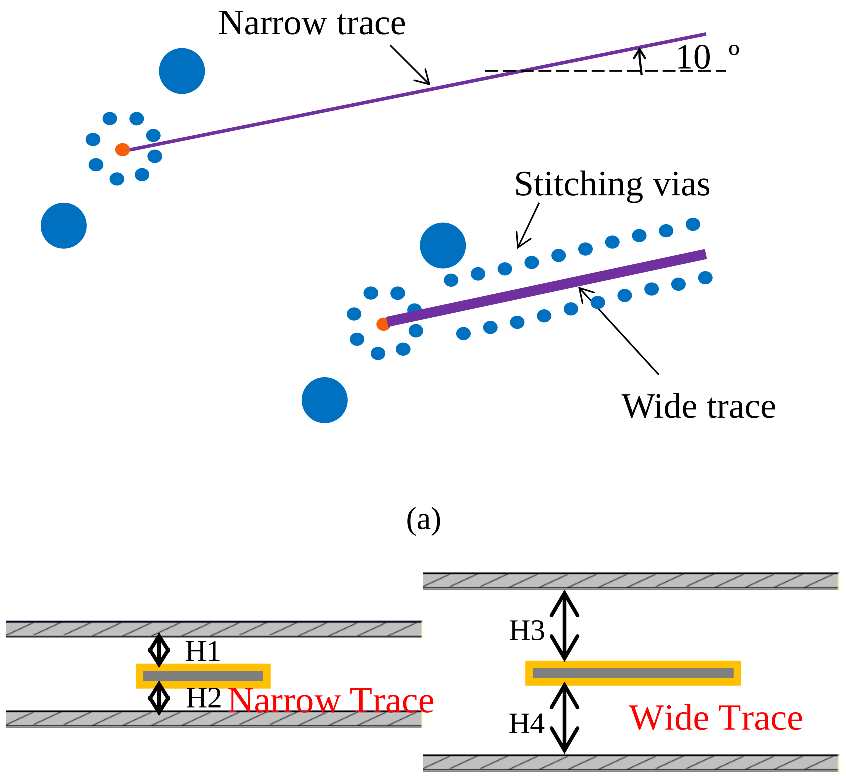

(a)

(b)

Figure 1 (a) Top view of the traces with different widths, with the broad trace also having shielding vias (b) Cross-sectional view of the two traces with different widths

2.1. TRL CALIBRATION AND MEASUREMENT RESULT

The TRL calibration standard, as is shown in Fig. 2, includes a ‘load’ standard, three ‘line’ standards with different lengths, a ‘thru’, and a ‘short’ standard. Each ‘line’ standard corresponds to a specific frequency range. For calculating the standard lengths, the relative permittivity ε_r is set as 3.83 based on the preliminary estimations of the DK on the manufactured test vehicles. The TRL calibration standards are designed up to 50 GHz.

The TDR measurements of all the standards are shown in Fig. 3. The TDR response starts from the connectors, followed by the vias and a small part of the 50-Ω trace. This step, before the TRL calibration, ensures that there are no issues with the mechanical connections or connector performance, as the TRL calibration assumes the same port effect for every measurement. Fig. 3 shows that the multiple 2.4-mm connectors used in this study behave similarly, and the connector impedances are close to 50 Ω. The two big bumps in Fig. 3 come from the inductive via, due to a layout error leading to higher via impedance. This limits the frequency range of reliable measurements to 20 GHz. However, extrapolation of the results to the higher frequencies is possible.

As the test lines have different cross-sections and reference layers, two separate TRL standards are used. The measured after calibration S-parameters for both the narrow and the wide traces are shown in Fig. 4. The loss for the wider trace is smaller than that of the narrow trace, as the conductor loss is inversely proportional to the cross-section area of the traces.

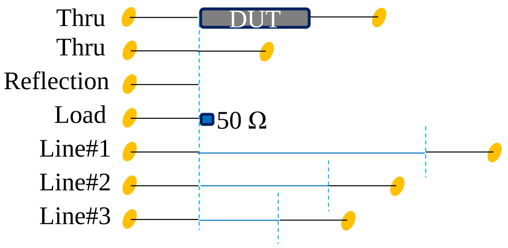

Assuming that $\varepsilon_r = 3.83$

Trace	Start Freq	Stop Freq	Total Length (connector to connector)
Thru	Low Frequency	50 GHz	600 mil
Reflection	Low Frequency	50 GHz	300 mil
Load	Low Frequency	281.2 MHz	300 mil
Line 1	281.2 MHz	1.581 GHz	2220.2 mil
Line 2	1.581 GHz	8.891 GHz	888.1 mil
Line 3	8.891 GHz	50 GHz	651.2 mil

Figure 2 TRL calibration standard details

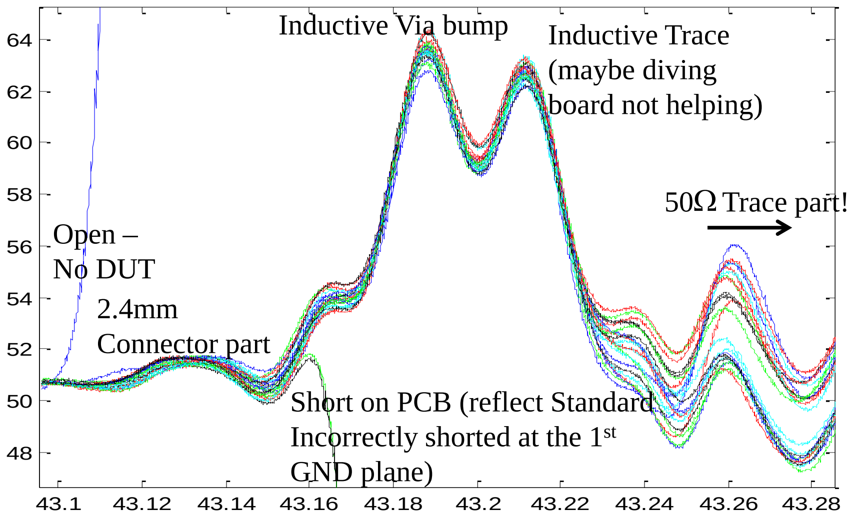

Figure 3 TDR measurement of all TRL standards and the DUT showing two big bumps representing the inductive via

2.2. METHODOLOGY FOR MATERIAL PROPERTY EXTRACTION FROM MEASUREMENT S-PARAMETER

The “root-omega” method for extracting material parameters in [3] assumes that the conductors are smooth, so all the effects of the conductor roughness are lumped into the dielectric properties. The dielectric properties, thus extracted, are not purely from the dielectric material. The method in [1] shows how the dielectric and conductor effects contribute to the total attenuation constant. This provides a way to separate the conductor roughness effect from the dielectric parameters. An overview of the material parameter extraction methodologies is shown in the flowchart in Fig. 5.

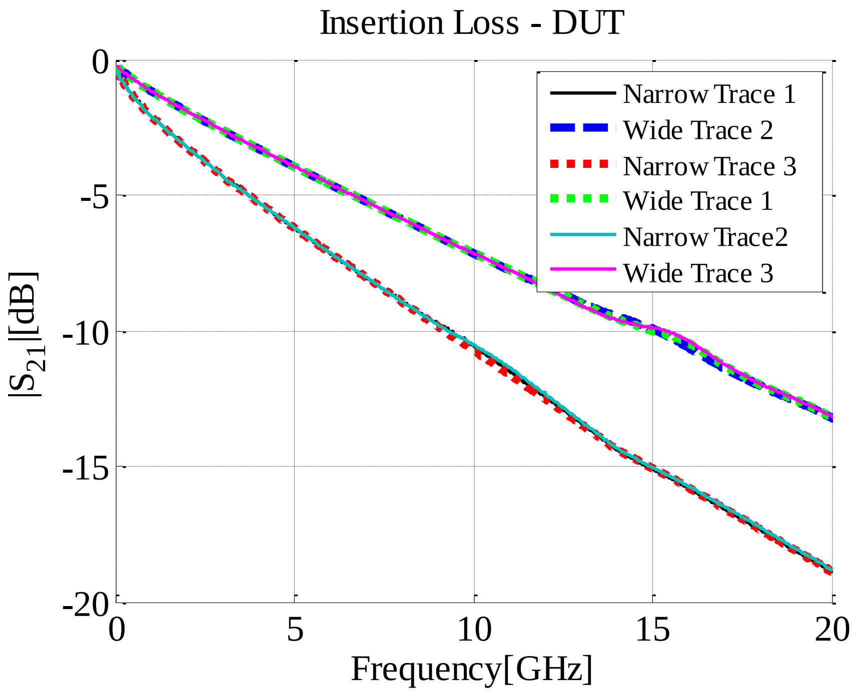

(a)

Figure 4 S-parameters of two traces over several repetitions of measurements (a)Two |S21| groups for narrow and wide trace each, (b) The return loss |S11| for the measurements is always below -20dB, (c) Phase of S21for all measurements of both traces is same as both are 50-Ohm striplines

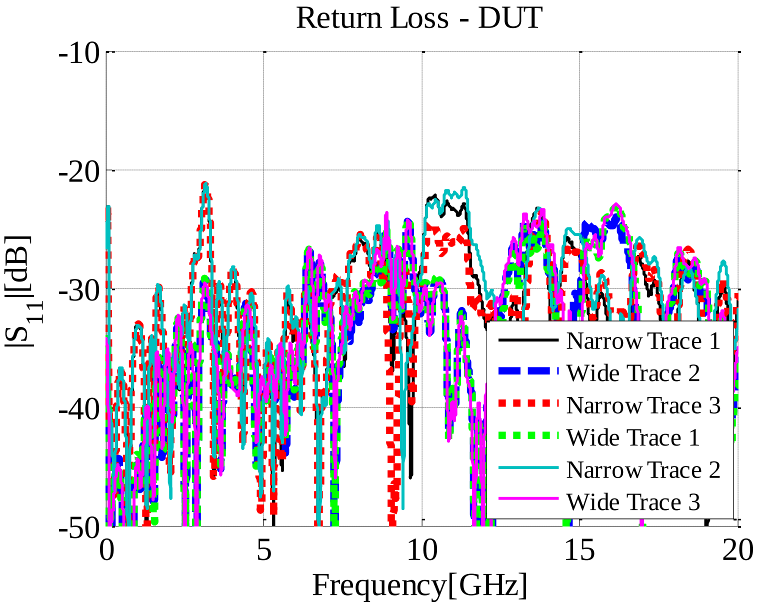

(b)

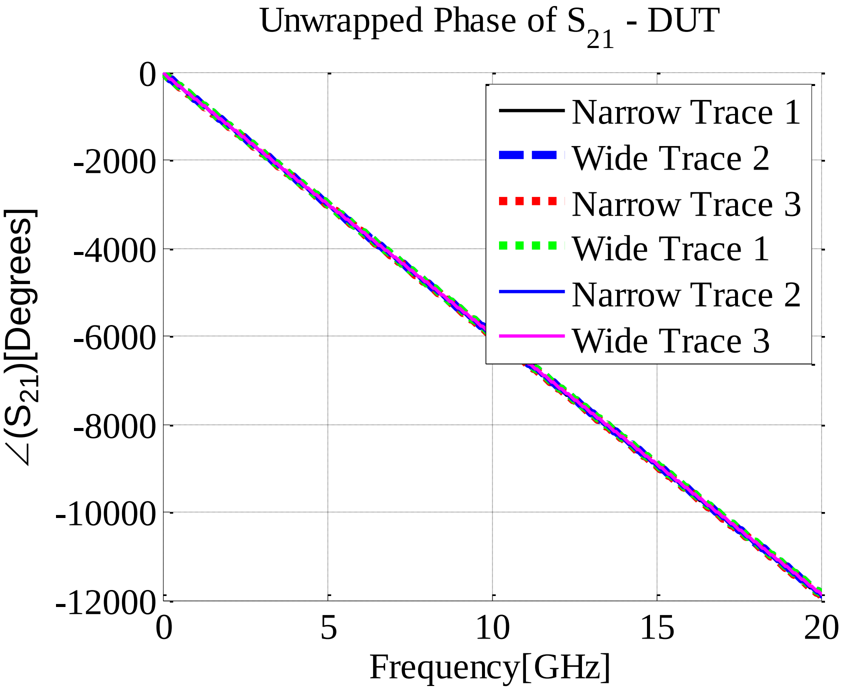

(c)

Figure 4 S-parameters of two traces over several repetitions of measurements (a)Two |S21| groups for narrow and wide trace each, (b) The return loss |S11| for the measurements is always below -20dB, (c) Phase of S21for all measurements of both traces is same as both are 50-Ohm striplines (Cont.)

The complex propagation constant γ for the transmission line can be obtained by converting the measured S-parameters into ABCD parameters, and using

$$\gamma = \frac{\operatorname{arccos}h(\sqrt{A\cdot D})}{linelength};\ \text{and}\ \gamma = \alpha_T + j\beta_T \tag{1}$$

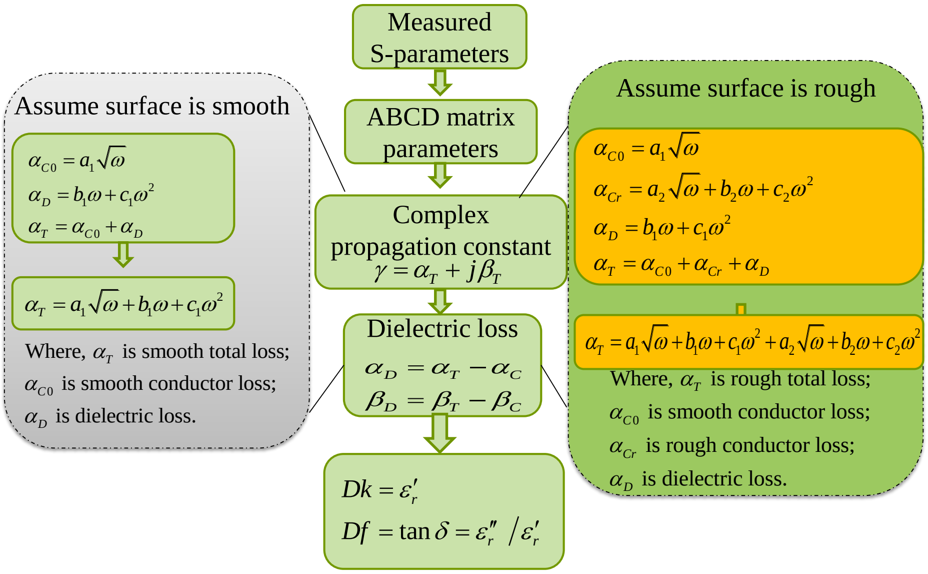

Figure 5 Methodology of material property extraction with the thread on the left assumes the conductor is smooth (root omega method) and the thread on the right accounts for roughness and separates it from the dielectric parameters

where, α_T is the total attenuation constant and β_T is the total phase constant. The total attenuation constant α_T is comprised of the conductor loss α_C and the dielectric loss α_D, thus,

$$\alpha_T = \alpha_C + \alpha_D \tag{2}$$

Two methods to obtain the material properties from the complex propagation constant are shown in the flowchart (Fig. 5). The left one is the root-omega method, and the one on the right takes into account conductor roughness.

Once the attenuation constant α_D and phase constant β_D for the dielectric are found from each method, the real and imaginary parts of permittivity are found in [5] as

$$\begin{array}{l} \beta_D = \frac{\omega}{c}\sqrt{\varepsilon_r} \times \cos(\delta/2) \\ \alpha_D = \frac{\omega}{c}\sqrt{\varepsilon_r} \times \sin(\delta/2) \text{, or} \\ \varepsilon_r = \sqrt{(\varepsilon_r')^2 + (\varepsilon_r'')^2} \end{array} \begin{cases} \varepsilon_r' = x\sqrt{\frac{x}{x+y}} \text{ and } \varepsilon_r'' = x\sqrt{\frac{y}{x+y}} \\ x = (\frac{\beta_D c}{\omega})^2 \text{ and } y = (\frac{2c\alpha_D}{\omega})^2 \end{cases} \tag{3}$$

where c is the speed of light in vacuum and ω is the angular frequency.

2.2.1. "Root-omega" Method. The total attenuation constant αT can be fitted to the equation,

$$\alpha_T = a\sqrt{\omega} + b\omega + c\omega^2 \tag{4}$$

where a, b, and c are the coefficients found from curve fitting. If the conductors on the PCB are assumed to be perfectly smooth, *i.e.*, the loss is only due to the skin-effect loss α_c and the dielectric loss α_D, then

$$\alpha_C = a\sqrt{\omega}\,, \;\; \alpha_D = b\omega + c\omega^2 \tag{5}$$

Then, the dielectric loss is found using (3). The dielectric constant is found from the measured total phase constant β_T, assuming that the conductor does not affect delay on the line ($\beta_D = \beta_T$). These simple assumptions are not quite correct at the frequencies, where conductor roughness starts playing an important part.

2.2.2. Assume the Conductors are Rough. Generally, the real PCBs with substantially rough conductors include not only the skin effect loss, and the dielectric loss, but also the rough conductor loss,

$$\alpha_{Cr} = a_2\sqrt{\omega} + b_2\omega + c_2\omega^2 \tag{6}$$

So that the actual total attenuation constant α_T can be represented as,

$$\begin{aligned} \alpha_T &= \alpha_{C0} + \alpha_D + \alpha_{Cr} \\ &= \boxed{a_1\sqrt{\omega}} + \boxed{b_1\omega + c_1\omega^2} + \boxed{a_2\sqrt{\omega} + b_2\omega + c_2\omega^2} \\ &= (a_1 + a_2)\sqrt{\omega} + (b_1 + b_2)\omega + (c_1 + c_2)\omega^2 \end{aligned} \tag{7}$$

Thus, the dielectric loss α_D can be calculated from equation (7), if α_T, α_{C0}, and α_{Cr} are known.

The S-parameter measurements of the narrow trace and wide trace are used to get the total attenuation constants α_T^N, α_T^W, respectively. Each can be curve fitted to get,

$$\begin{aligned} \alpha_T^W &= K_1^N\sqrt{\omega} + K_2^N\omega + K_3^N\omega^2 \\ &= \left(a_1^N + a_2^N\right)\sqrt{\omega} + \left(b_1^N + b_2^N\right)\omega + \left(c_1^N + c_2^N\right)\omega^2 \end{aligned} \tag{8}$$

$$\begin{aligned} \alpha_T^W &= K_1^W\sqrt{\omega} + K_2^W\omega + K_3^W\omega^2 \\ &= \left(a_1^W + a_2^W\right)\sqrt{\omega} + \left(b_1^W + b_2^W\right)\omega + \left(c_1^W + c_2^W\right)\omega^2 \end{aligned} \tag{9}$$

where, $K_1 = a_1 + a_2$, $K_2 = b_1 + b_2$, and $K_3 = c_1 + c_2$ are the curve fitted coefficients for the total attenuation constant with the superscript 'N' for the narrow trace and 'W' for the wide trace.

As the number of unknowns is greater than the number of available equations, the sum and difference equations are used to eliminate the like terms for the narrow and wide trace attenuation constants. Also, as the surface roughness of copper, and, the surrounding dielectric material, is the same for both traces, most of the terms, if not equal, can be expressed in terms of the ratios of trace cross-sectional dimensions. The subtraction and summation of the $\sqrt{\omega}$ term of (8) and (9), gives,

$$\begin{cases} K_1^N - K_1^W = a_1^N\left(1-\dfrac{a_1^W}{a_1^N}\right)+a_2^N\left(1-\dfrac{a_2^W}{a_2^N}\right) \\ K_1^N + K_1^W = a_1^N\left(1+\dfrac{a_1^W}{a_1^N}\right)+a_2^N\left(1+\dfrac{a_2^W}{a_2^N}\right) \end{cases} \tag{10}$$

The coefficients corresponding to the dielectric loss can be assumed to be the same, since the dielectric material surrounding the traces is the same, $b_1^N = b_1^W$, $c_1^N = c_1^W$.

The difference of the ω and ω^2 term of (8) and (9),

$$K_2^N - K_2^W = b_2^N\left(1-\frac{b_2^W}{b_2^N}\right) \tag{11}$$

$$K_3^N - K_3^W = c_2^N\left(1-\frac{c_2^W}{c_2^N}\right) \tag{12}$$

The ratios of coefficients are the function of the trace geometry and roughness, as

$$\begin{cases} \dfrac{a_1^W}{a_1^N} = \dfrac{P^N}{P^W} \\ \dfrac{a_2^W}{a_2^N} = \dfrac{\left(A_1^W/w_1^W + A_2^W/w_2^W\right)\times t^N}{\left(A_1^N/w_1^N + A_2^N/w_2^N\right)\times t^W} \\ \dfrac{b_2^W}{b_2^N} = \dfrac{P^N}{P^W}\times\dfrac{\left(A_1^W/\Lambda_1^W + A_2^W/\Lambda_2^W\right)}{\left(A_1^N/\Lambda_1^N + A_2^N/\Lambda_2^N\right)} \\ \dfrac{c_2^W}{c_2^N} = \dfrac{P^N}{P^W}\times\dfrac{\left(A_1^W/\Lambda_1^W + A_2^W/\Lambda_2^W\right)}{\left(A_1^N/\Lambda_1^N + A_2^N/\Lambda_2^N\right)} \end{cases} \tag{13}$$

where, P is the cross-sectional perimeter on the trace, A is the peak-to-valley roughness amplitude, Λ is the peak-to-peak roughness period, t is the trace cross-sectional thickness, and w is the trace cross-sectional width, as are shown in Fig. 6. The superscripts 'N' and 'W' are used to represent the narrow trace and the wide trace, respectively, and the roughness parameter subscripts '1' and '2' represent the oxide side and the foil side of the traces, respectively.

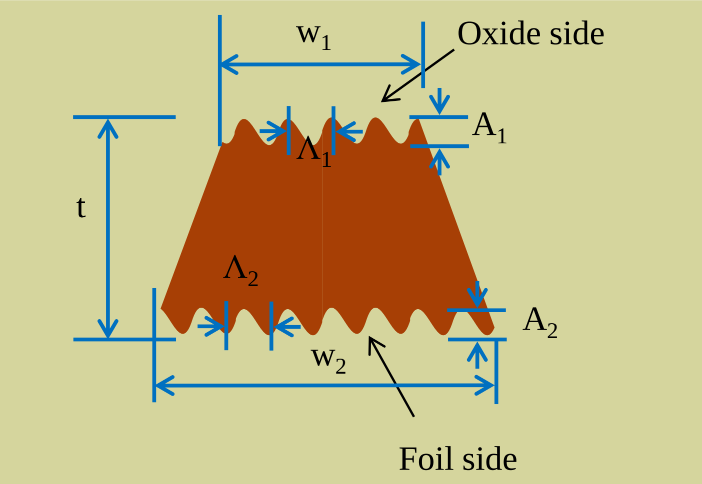

Figure 6 Rough conductor cross-section showing the different dimensions and roughness parameters

The skin effect loss, α_{C0}, and hence a_1 is inversely proportional to the trace cross-sectional perimeter (P) of the two traces. The $\sqrt{\omega}$ coefficient in rough conductor, a_2, represents the skin effect loss due to the extra surface area, not accounted for in α_{C0}, hence directly proportional to the roughness amplitude (A) normalized by the thickness (t) and the width (w) of the traces for both sides of the trace. The coefficients of ω and ω^2, b_2 and c_2, are associated some effective roughness dielectric medium, which is composed of the conductor particles embedded in the dielectric matrix (epoxy resin) in certain proportions [6].

The latter depends on the values of the roughness amplitude (A) and the roughness period (Λ). The ratios b_2^W / b_2^N and c_2^W / c_2^N are proportional to the P, Λ and A values as shown in (12) [1],[7].

Assuming these stripline cross-sectional dimensions are known accurately, all the coefficients in (7) can be resolved by substituting the ratios from (13) in (10), (11) and (12). Thus, the dielectric loss constant α_D can be found using b1 and c1. Then, dielectric phase constant β_D can be calculated with the same method as used for the dielectric attenuation constant α_D. Using the dielectric loss α_D and the dielectric phase β_D in (3), the refined dielectric constant Dk and the dissipation factor Df are calculated.

3. RESULTS AND DISCUSSION

Three individual cross-sectional samples are made of each trace for the analysis. The values of trace cross-sectional dimensions and the surface roughness parameters are averaged over the optical measurements of the three samples. One of the cross-sections of the stripline with the narrow trace is shown in Fig. 7. The average values of the side dimensions and parameters over the three trace cross-section samples are shown in Table. 1.

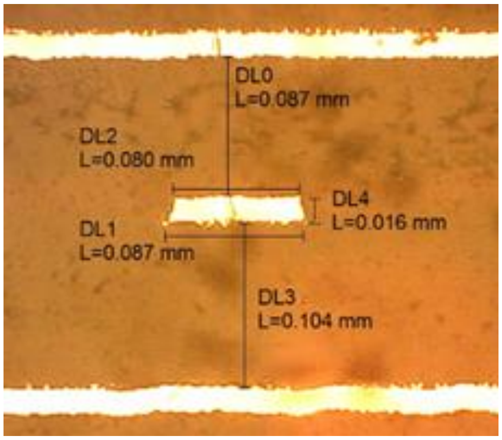

Figure 7 Narrow trace cross-section observed under a metallographic microscope shows the trace and reference planes with the relevant dimensions marked on the image

Table 1Values of the Trace Cross-Sectional Analysis Parameters Averaged Over the Measurements from Three Samples

	P (um)	t (um)	W_1	W_2	A_1	A_2	Λ_1	Λ_2
Narrow trace	193	16	78	212	3.473	3.773	27.223	32.673
Wide trace	461	16	84	218	3.505	3.756	21.133	22.86

The dielectric constant Dk and the dissipation factor Df values are calculated using the dimensions and surface roughness parameters listed in Table I, and the procedure is outlined in Section II(b). Figs. 8 and 9 show the Dk and the Df as functions of frequency, when the "root-omega" on each trace and the proposed method on both traces are used.

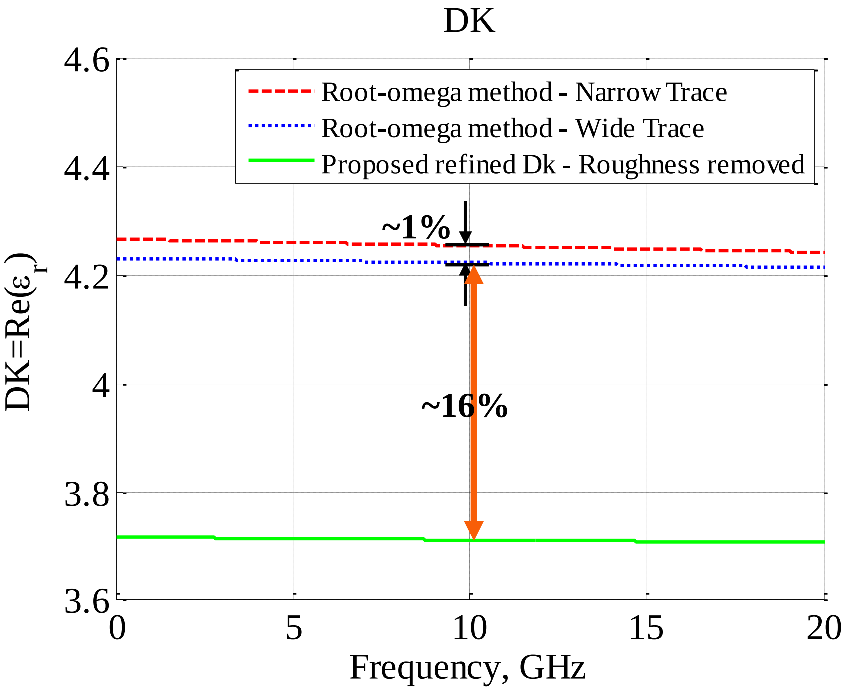

Figure 8 Dk found using root omega method and proposed new method with a difference of about 16% between the two methods at 10 GHz

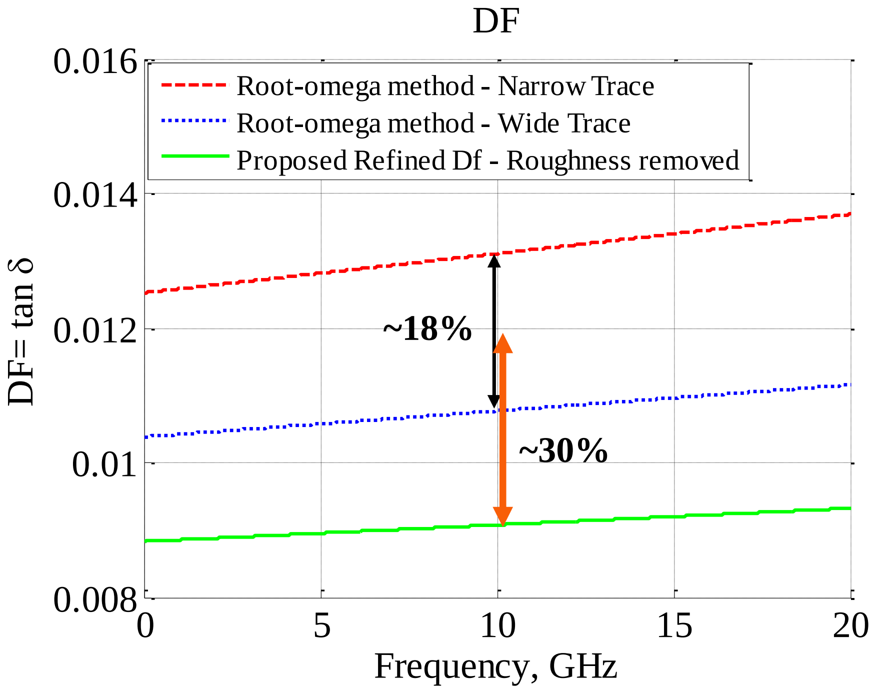

Figure 9 Dk found using root omega method and proposed new method with a difference of about 18% in root omega method results from different traces and 30% between the two methods at 10 GHz

The dash and the dot curves represent results of the narrow trace and the wide trace, respectively, in the Fig. 8 and Fig. 9. These are calculated with the root-omega method, so the roughness effect is embedded in the dielectric. Here, the Df for narrow trace (green) is higher than that for the wider trace (red), as the narrow trace is affected more by the surface roughness loss lumped into the dielectric loss. The results show an ambiguity in Df when calculated from traces of different widths, about 18% over the average at 10 GHz. The Dk has relatively good agreement, less than 1%.

The green solid curve represents the refined ambient effective Dk and Df, calculated using the proposed method in Section 2.2.2. As the measurements on both traces are used for calculations, the unique result (no ambiguity) is obtained. When the effect of surface roughness is removed, both the Dk and Df reduce significantly. The resultant Df value is lower than both results of the “root-omega” method, as the conductor roughness effect is not lumped in Df anymore. If the average values of the “root omega” method results are used, then the discrepancies in the Dk and Df estimation for lines with the narrow and wide traces at 10 GHz are about 16% and 30%, respectively.

As the accuracy of the extracted data depends on the S-parameter measurements, it is important to discuss the sources of error in measurements. The connectors need to be mounted carefully so that their TDR response is the same, which minimizes the error in the TRL calibration. This depends on many factors like the similarity in performance of each connector by itself, the degree of tightening of the mounting screws, the connection resistance, the cable to connector mating irregularities, etc. The error from the calibration may affect the behavior of the S-parameters, and hence generate errors in the curve fitting.

Another source of errors is the optical measurement for the trace dimensions and surface roughness parameter extraction, which is sensitive to the sample preparation. The trace cross- section should be exactly perpendicular to the trace direction. If a cross-section is titled, each dimension measurement may be inaccurate. Also the polishing process to get a smooth surface to observe under the microscope may affect the roughness profile. Thus, the reliability of the peak-to-valley roughness amplitude A and the peak-to-peak roughness period Λ values depend on the sample preparation process. Also the ratios of dimensions or roughness parameters, which are used for estimation of coefficients standing before the $\sqrt{\omega}$, ω, and ω^2 terms, are empirical ratios, retrieved from multiple, but still limited experimental data points. This may introduce some uncertainty in the calculation of the resulting coefficients, which determine the Df extraction.

This method can be compared with some previous work if the test vehicles are made from the same dielectric material and conductor combinations. Such comparison is difficult as, so far, all the methods were used with traces on different boards, which may have different material properties and roughness due to the different suppliers and manufacturing variance. More test vehicles are in the pipeline to be able to compare with some known data points.

As a future direction, another self-consistency method can be devised to have three traces of different widths in a test board, on the same layer. Then three combinations of two traces are available for use to find the material parameters. The third trace could be used to verify the results by comparing predicted S-parameter results with the measured results. This method is similar to the DERM method [4] with three boards, except in this case, all traces are on one board reducing the manufacturing variance.

4. CONCLUSION

The proposed method uses two stripline traces in the same layer of the PCB to find the values of refined ambient effective Dk and Df of the dielectric. The values of Dk and Df were found using two methods, the “root-omega” method and the proposed two-stripline method which accounts for and removes the effect of surface roughness. The “root–omega” method lumps the conductor roughness into dielectric properties and creates an ambiguity in the dielectric properties extracted from traces of different widths. The proposed method provides the Dk and Df refined from the conductor roughness, and hence a unique result. The values of Dk and Df are shown to be lower than those obtained using the “root-omega” method. The value of Dk is closer to the manufacturer’s ratings of 3.8. Also, the lower Df is reasonable as now it does not account for the loss due to surface roughness.

The difference in the Dk and Df values after removing the surface roughness effect is significant enough to affect the SI and PI simulations results. The proposed method provides a way to separate the effect of roughness and highlights the importance of addressing roughness loss for high frequency PCB applications.

BIBLIOGRAPHY

[1] M.Y. Koledintseva, A. Koul, S. Hinaga, and James L. Drewniak. "Differential and extrapolation techniques for extracting dielectric loss of printed circuit board laminates." in *Microwave Symposium Digest (MTT), 2011 IEEE MTT-S International*, Baltimore, MD, 2011, pp. 1-4.

[2] E. Bogatin, S. Begley, and M. Resso, "The role of dielectric constant and dissipation factor measurements in multi-gigabit systems." *DesignCon*, 2007, San Jose, CA, Feb. 2007.

[3] Koul, P. K. R Anmula, M. Y. Koledintseva, J. L. Drewniak, and S. Hinaga. "Improved technique for extracting parameters of low-loss dielectrics on printed circuit boards." in *Proc. IEEE Symp. Electromag. Compat.,* Aug. 17-21, Austin, TX, 2009, pp. 191-196.

[4] Koul, M. Y. Koledintseva, S. Hinaga, and J. L. Drewniak. "Differential extrapolation method for separating dielectric and rough conductor losses in printed circuit boards." *Electromagnetic Compatibility, IEEE Transactions,* vol. 54, no. 2, pp. 421-433, 2012.

[5] J. R. Miller, G. Blando, and I. Novak. "Additional trace losses due to glass-weave periodic loading." in *Proceedings of DesignCon*, pp. 1-4. 2010.

[6] M.Y. Koledintseva, A. Razmadze, A. Gafarov, S. De, S. Hinaga, and J.L. Drewniak, "PCB conductor surface roughness as a layer with effective material parameters." *IEEE Symp. Electromag. Compat.*, Pittsburg, PA, 2012, pp. 138- 142.

[7] M. Koledintseva, J. Drewniak, S. Hinaga, F. Zhou, A. Koul, and A. Gafarov, "Experiment-based separation of conductor loss from dielectric loss in striplines." *DesignCon 2011,* Santa Clara, CA, Jan. 31-Feb. 3, 2011, paper 5-TP5.

VITA

Lei Hua was born in Heibei, China. In July 2001, she obtained a bachelor’s degree in College of Biochemical Engineering from East China University of Science and Technology, Shanghai, R.P. China.

In August 2011, she enrolled at Missouri University of Science and Technology to pursue a master’s degree of Electrical and Computer Engineering under the guidance of Dr. Hai Xiao. Her research interest is RF based devices and fiber optic sensors.